

1 **Measurement report: Insights into the high temporal variability of**
2 **atmospheric carbon dioxide (CO₂) at a suburban station in the Indo-**
3 **Gangetic Plain**

4

5 Vimal Jose Vazhathara^{1, *}, Ravi Kumar Kunchala¹, Sajeev Philip¹, Jaswant Rathore¹, Dilip
6 Ganguly¹, Sagnik Dey^{1,2}, [Tomoki Nakayama³](#), Yutaka [Matsumi^{4,5}](#) and Prabir K. [Patra^{4,6}](#)

7

8 ¹Centre for Atmospheric Sciences, Indian Institute of Technology Delhi, New Delhi, India.

9 ²Centre of Excellence for Research on Clean Air, Indian Institute of Technology Delhi, New
10 Delhi, India

11 [³Graduate School of Integrated Science and Technology, Nagasaki University, 1-14 Bunkyo-](#)
12 [machi, Nagasaki, Nagasaki, 852-8521, Japan](#)

13 [⁴Research Institute for Humanity and Nature, Kyoto, Japan](#)

14 [⁵Institute for Space-Earth Environmental Research, Nagoya University, Nagoya, Japan](#)

15 [⁶Japan Agency for Marine-Earth Science and Technology \(JAMSTEC\), Yokohama, Japan.](#)

16 *Correspondence to: Vimal Jose Vazhathara (vimaljosevazhathara@gmail.com), Centre for
17 Atmospheric Sciences, Indian Institute of Technology Delhi, New Delhi, 110016, India

18

19 **Abstract**

20 The unusual weather patterns and large anthropogenic emissions over the Indo-Gangetic Plain
21 (IGP) make it a significant hotspot of greenhouse gases like carbon dioxide (CO₂). Given the
22 significance of the IGP and highly populated Delhi National Capital Region (Delhi-NCR), a
23 GHG observatory was established at a suburban monitoring station in Sonipat, Haryana
24 (28.95°N, 77.10°E; 228m asl), about 45 km north of the Delhi state boundary. Using a laser-
25 based cavity ring-down spectroscopy (CRDS) technique, we measured CO₂ mole fraction from
26 February 2023 to January 2025. An annual average CO₂ mole fraction of 440.8±19.7 parts per
27 million (ppm) was recorded in 2024, which includes a strong seasonal variability, ranging from

Deleted: Matsumi^{3,4}

Deleted: Patra^{3,5}

Deleted: ³Research

Deleted: ⁴Institute

Deleted: ⁵Japan

33 422.6±23.3 ppm during the monsoon (June- September) to 456.4±30.8 ppm in post-monsoon
34 (October -November). A strong CO₂ diurnal amplitude of 29 ppm in May and 63 ppm in
35 October was observed mainly due to seasonal changes in boundary layer mixing (faster in May
36 than October) and biospheric activity (weaker in May than October). Further investigation of
37 the drivers of strong seasonal and diurnal CO₂ variability over IGP revealed a strong contrast
38 to other global monitoring stations in the same latitude band. A strong correlation between CO₂
39 and methane (CH₄) indicated a co-located emission source, while the strong positive correlation
40 between CO₂ and carbon monoxide (CO) during post-monsoon emerges due to emissions from
41 biomass burning. We demonstrated that the high temporal CO₂ variability in the IGP region is
42 driven by the complex interplay of local anthropogenic and biomass burning emissions,
43 biospheric fluxes, and prevailing meteorology.

44

45 1. Introduction

46 Carbon dioxide (CO₂) is the major greenhouse gas (GHG) contributing to climate change and
47 global warming (IPCC, 2021; Fawzy et al., 2020). Due to the long lifetime and high radiative
48 forcing potential, CO₂ can have a significant impact on global and regional climate (Wang et
49 al., 2010). The atmospheric CO₂ mole fraction has increased from 278 parts per million (ppm)
50 in the pre-industrial period to 427 ppm in 2025 (NOAA, <https://gml.noaa.gov>; Wigley (1983).
51 This rapid increase in the atmospheric fraction of CO₂ is primarily due to the combustion of
52 fossil fuels, cement manufacture, deforestation, and other industrial processes (Stocker et al.,
53 2013; Huang et al., 2016; Yoro and Daramola, 2020). A comprehensive understanding of the
54 sources and sinks of CO₂ is critical for developing national policies to mitigate climate change
55 impacts.

56 India is the third-highest CO₂-emitting nation (8% of total global CO₂) in the last
57 decade, as reported by the Global Carbon Project (GCP) (Friedlingstein et al., 2025; Le Quéré
58 et al., 2018). In particular, the Indo-Gangetic Plain (IGP) region is one of the hotspots of
59 atmospheric CO₂ mole fraction, primarily due to large fossil fuel emissions and adverse
60 meteorology (Halder et al., 2021; Krishnapriya et al., 2025; Kuttippurath et al., 2022). Over the
61 past few decades, the IGP region has witnessed rapid urbanisation, industrialisation, and
62 agricultural intensification, leading to significant changes in land-use patterns and GHG
63 emissions (Yoro and Daramola, 2020). Mitigation of anthropogenic CO₂ emissions in the
64 highly populated IGP region is crucial to reducing the build-up of atmospheric CO₂ mole

Deleted: to

Deleted:

67 fractions. Gaining a better understanding of the magnitude of CO₂ sources and sinks and the
68 local drivers of CO₂ temporal variability over the IGP region is therefore important.

69
70 Continuous monitoring of ground-based CO₂ is of utmost importance for inverse
71 modelling approaches to understand local-to-regional-scale sources and sinks of CO₂.
72 Although GHG mole fractions have been monitored worldwide for decades, GHG monitoring
73 stations in India are limited (Kunchala et al., 2025; Chakraborty et al., 2020; Kumar et al.,
74 2021; Patra et al., 2013; Tiwari et al., 2013). The Cape Rama (15.08° N, 73.83° E) station,
75 situated on India's southwest coast, was the first Indian monitoring station to track CO₂ mole
76 fraction from 1993 to 2002 (Bhattacharya et al., 2009; Patra et al., 2011; Rayner et al., 2008).
77 Recently, several monitoring stations have been established over different parts of India to
78 measure the GHGs (Chandra et al., 2016; Jain et al., 2021; Mahesh et al., 2015; Metya et al.,
79 2021; Nomura et al., 2021; Pathakoti et al., 2023; Sreenivas et al., 2016; Thilakan et al., 2023;
80 Tiwari et al., 2014). Studies have also been conducted using aircraft-based measurements
81 (Niwa et al., 2012; Patra et al., 2011; Schuck et al., 2012; Zhang et al., 2007) and satellite data
82 products (Das et al., 2023; Kunchala et al., 2022; Nalini et al., 2019; Philip et al., 2022; Xiong
83 et al., 2009). The incorporation of regional in situ and aircraft-based measurements, along with
84 satellite columnar CO₂ retrievals, reduced uncertainties in top-down CO₂ flux estimates (Huang
85 et al., 2008; Niwa et al., 2012; Zhang et al., 2014).

86 To comprehensively understand temporal CO₂ variability and its drivers in the western
87 IGP region, we have conducted atmospheric CO₂ mole fraction measurements at Sonipat, a
88 suburban station in the IGP region upwind of Delhi. The continuous measurements from
89 February 2023 to January 2025 were conducted using laser-based cavity ring-down
90 spectroscopy. Here, we investigate the novel characteristics of the seasonal and diurnal
91 variability of atmospheric CO₂ mole fraction at Sonipat. We then identify the key drivers of
92 the observed temporal CO₂ variability in the region.

93

94 **2. Materials and methods**

95 **2.1 Monitoring station**

96 The measurements in this study were carried out at the Indian Institute of Technology Delhi
97 (IIT Delhi) Centre for Atmospheric Sciences (CAS) - Atmospheric Observatory situated at
98 Sonipat campus (28.95°N, 77.10°E, 228m asl). Sonipat is an upwind suburban region of the
99 Delhi-NCR, situated in the northern Indian state of Haryana, approximately 45 kilometres north
100 of Delhi. The monitoring station is surrounded by agricultural fields, a National Highway, and

101 academic institutions (Rathore et al., 2025). Figure 1 shows the location map of the monitoring
102 station. The climatic conditions over this site are similar to Delhi which has sweltering
103 summers (March-May), damp or moist monsoons (June - September), and extreme winters.
104 Similar to Delhi, this region also has frequent haze and smog with low visibility during winter
105 (December - February) and post-monsoon (October - November) seasons. During the post-
106 monsoon season, Sonipat experiences large transport of pollutants from the North-West
107 direction. In addition to the pollutant transport, several local emission sources exist in the
108 region, such as small industries, vehicular sources, and local biomass burning affecting short-
109 lived air pollutants (Rathore et al., 2025).

110

111 **2.2 Local measurements**

112 **2.2.1 GHG measurements**

113 This study utilised the PICARRO G2301 GHG analyser to measure major atmospheric GHG
114 mole fractions. The PICARRO analyser employs the Cavity Ring-Down Spectroscopy (CRDS)
115 technique at 0.5 Hz to measure CO₂ mole fraction. The CRDS technique utilises the ring-down
116 time of light intensity within the cavity to determine the mole fraction of CO₂, a method
117 fundamentally different from other measurement techniques such as Non-dispersive Infrared
118 Spectroscopy (NDIR) and Fourier Transform Infrared Spectroscopy (FTIR). The long sample
119 interaction path length (approximately 20 km) is a characteristic of CRDS, which enhances
120 sensitivity compared to conventional techniques based on light-intensity absorption. The cavity
121 pressure operates at a very low pressure of 140 Torr. This isolates a single spectral feature with
122 a resolution of 0.0003 cm⁻¹, ensuring a linear relationship between peak height or area and mole
123 fraction. The CRDS provides precise, highly sensitive measurements of gases in ambient air
124 with a temporal resolution of 5 seconds. The technique has been well validated for measuring
125 atmospheric CO, CO₂, and CH₄ mole fractions globally and at some Indian monitoring stations
126 (Chandra et al., 2016; Chen et al., 2013; Jain et al., 2021).

127 The standard cavity temperature of 45°C (throughout the measurement period) ensures
128 the necessary etalon mechanical stability of the measurement cavity. The sample air was taken
129 from the top of the building and above the tree canopy (5 meters above the instrument housing)
130 through a Teflon (PTFE) tube with an inner diameter of 3 mm using an external vacuum pump
131 with ~400 SCCM flow rate (residence time ~5.9 s). The air intake height is about 248 m.

132 The Sonipat station, lying on the upwind side of Delhi, is a suburban station with
133 relatively cleaner air compared to the urban city centre. However, Sonipat cannot be considered
134 a pristine site due to the impact of local emissions from nearby industries and national

135 highways. We adopted (1) the fifth percentile of the daily data to characterise background mole
136 fraction at the site (Ammoura et al., 2014; Chandra et al., 2016; Jain et al., 2021), and (2) the
137 adaptive diurnal minimum variation selection (ADVS) method that considers the diurnal
138 minimum value as the daily background value (Apadula et al., 2019; Yuan et al., 2018). In this
139 study, the comparison between the fifth percentile and the ADVS methods showed similar CO₂
140 background values (see Fig. S1), and the ADVS method was used for further analysis. The
141 excess CO₂ mole fractions were then estimated by subtracting the hourly averaged values of
142 CO₂ from the background mole fraction.

143 The measurements of the atmospheric CH₄ mole fraction were also conducted with the
144 PICARRO G2301 GHG analyser. The GHG analyser employs the CRDS at 0.5 Hz to measure
145 CH₄ mole fraction. The mole fractions of CH₄ were determined using the ring-down time of
146 light intensity, similar to CO₂ mole fractions. Calibration was performed following the
147 guidelines of the National Oceanic and Atmospheric Administration Earth System Research
148 Laboratories (NOAA-ESRL, 2020) and the Integrated Carbon Observation System (ICOS)
149 protocol (Laurent, 2020), using NOAA standard calibration cylinders. Further details of the
150 calibration process are provided in Supplementary Section S1.

Deleted: 2016

151

152 2.2.2 Trace gas measurements

153 In addition to the measurements of CO₂ and CH₄, we also utilised the measurements of trace
154 gases to establish the species interrelationships and to identify drivers of GHG sources. We
155 used a compact air-quality measurement instrument with gas sensors (CUPI-G) to continuously
156 measure air pollutants, including fine particulate matter (PM_{2.5}), nitric oxide (NO), nitrogen
157 dioxide (NO₂), and carbon monoxide (CO). The sensors used in CUPI-G are a palm-sized
158 optical PM_{2.5} sensor developed by Panasonic, a CO-B4 Carbon Monoxide Sensor, and an NO-
159 B4 Nitric Oxide Sensor, developed by Alphasense. The sensitivity of the PM_{2.5} and CO sensors
160 was evaluated in Nagasaki, Japan, through intercomparisons with reference-grade instruments
161 employing a beta attenuation monitor (BAM) for PM_{2.5} and non-dispersive infrared (NDIR)
162 spectroscopy for CO measurements (Figure S1). The estimated unit-to-unit variability was 29%
163 for PM_{2.5} sensors and 21% for CO sensors. Further details on the sensor specifications and the
164 calibration methodology are described in Mangaraj et al. (2025).

Deleted: the

Deleted: the

Deleted: , respectively.

Deleted: (courtesy of Prof. Tomoki Nakayama),

Deleted: .

165

166 2.2.3 Local meteorology measurements

167 A Vaisala Ceilometer lidar CL61 provides real-time measurements of cloud base height (CBH)
168 for up to five layers, along with depolarisation measurements, under all weather conditions. To

175 determine the Planetary boundary layer height (PBLH) from the range-corrected attenuated
176 backscatter data, the gradient method (Summa et al., 2013) and the Wavelet Covariance
177 Transform (WCT) method (Baars et al., 2008) were employed. Further details on PBLH
178 calculations can be found in Rathore et al., (2025). An automatic weather station (AWS) by
179 Geonica, installed on the I-Tech building rooftop, collected meteorological data at 5-minute
180 intervals. The data, including ambient temperature, relative humidity (RH), atmospheric
181 pressure, wind speed and direction, precipitation, and incoming solar radiation, were retrieved
182 using Datagraph-W4K 2.1.3.0 software and exported in CSV format. All sensors were
183 meticulously calibrated and regularly cleaned to ensure accuracy and reliability.

184

185 **2.3 Auxiliary data**

186 **2.3.1 ObsPack Data**

187 To compare the seasonality of atmospheric CO₂ of Sonipat with other non-Indian sites in the
188 same latitudinal band, we used selected sites from the
189 obspack_co2_1_GLOBALVIEWplus_v10.1_2024-11-13 (Schuldt et al., 2024). The data was
190 averaged for five years from 2018 to 2022 for all stations except Boulder Atmospheric
191 Observatory, Colorado, (2011-2016), to compare the seasonality over different locations across
192 the globe.

193

194 **2.3.2 Satellite CO₂ retrievals**

195 Along with the ground-based in situ CO₂ measurements at the Sonipat monitoring station, we
196 also used column average dry air CO₂ mole fraction (XCO₂) retrievals from the Orbiting
197 Carbon Observatory-2 and 3 satellites (OCO-2 and OCO-3) (Crisp et al., 2017; Eldering et al.,
198 2017). We used the bias-corrected OCO-2 v11.1r data product for the period from February
199 2023 to December 2024. The OCO-3 satellite provides XCO₂ data at a repeat cycle of 16 days
200 with a spatial resolution of 1.60 km × 2.25 km (nadir observation), which increases the swath
201 area from ~3.0 km² to ~3.5 km². We used the bias-corrected OCO-3 v10.4r data product
202 (Eldering et al., 2019; Srivastava et al., 2020) for the period from February 2023 to December
203 2024.

204

205 **2.3.3 FluxSat GPP**

206 To study the Gross Primary Production (GPP) fluxes over Sonipat, we used FluxSat v2.2 native
207 GPP product computed at the spatio-temporal resolution of the MCD43C data set (daily at
208 0.05° spatial resolution (Schaaf et al., 2002; Wang et al., 2018). FluxSat v2.2 has been derived

209 from the MODerate resolution Imaging Spectroradiometer (MODIS) instruments on the NASA
210 Terra and Aqua satellites using the collection 6.1 MCD43C Bidirectional Reflectance
211 Distribution Function (BRDF)-Adjusted Reflectances (NBAR) (Joiner et al., 2018; Joiner and
212 Yoshida, 2020; Schaaf and Wang, 2021). FluxSat v2.2 is “calibrated” using a set of the
213 FLUXNET 2015 and OneFlux tier 1 (publicly released) eddy covariance (EC) data and has
214 been compared with independent data (i.e., not used in the calibration) as validation. We used
215 Global Gross Primary Production (GPP) estimates for 2023 in this study.

216

217 **2.3.4 Ecosystem-proxy variables**

218 We used two key ecosystem proxy variables to examine the carbon cycle dynamics at the
219 Sonipat station and in the IGP region. The Normalised Difference Vegetation Index (NDVI)
220 version 5 data from the Advanced Very High Resolution Radiometer (AVHRR) was used here
221 (Vermote and NOAA CDR Program, 2018). The NDVI CDR summarises surface vegetation
222 coverage activity based on measurements in the red and near-infrared spectral bands at daily
223 intervals and at a spatial resolution of $0.05^\circ \times 0.05^\circ$.

224 To understand the photosynthetic capacity of the regional ecosystem to assimilate
225 atmospheric CO₂, we used Solar-Induced Chlorophyll Fluorescence (SIF) retrievals from the
226 OCO-2 satellite (Frankenberg et al., 2014). The OCO-2 provides SIF data at a temporal
227 resolution of 16 days and a spatial resolution of $1.35 \text{ km} \times 2.25 \text{ km}$. The estimation of SIF
228 relies on evaluating the in-filling of solar Fraunhofer lines at 757 nm and 770.1 nm surrounding
229 the O₂ A-band (Frankenberg et al., 2014; Sun et al., 2018). We used bias-corrected SIF data
230 from OCO-2 v11r and v11.2r SIF data products.

231

232 **2.4 Models**

233 **2.4.1 JAMSTEC's MIROC version 4 atmospheric chemistry-transport model (MIROC4- 234 ACTM)**

235 We used the Model for Interdisciplinary Research on Climate version 4 (MIROC4),
236 atmospheric general circulation model (AGCM)-based chemistry-transport model (MIROC4-
237 ACTM; Patra et al., 2018), to simulate CO₂ mole fraction for this study. Simulations were
238 performed at a horizontal resolution of T42 spectral truncations ($\sim 2.8^\circ$ latitude–longitude grid)
239 with 67 vertical hybrid-pressure layers between the Earth's surface and 0.0128 hPa ($\sim 80 \text{ km}$).
240 CO₂ tracers were simulated corresponding to fossil fuel combustion (FFCO₂), land biosphere
241 fluxes (LBCO₂), fire emissions (CO_{2fire}), and ocean exchanges (CO_{2ocean}) from different prior
242 (bottom-up) emissions sets (Chandra et al., 2022). FFCO₂ was simulated using the gridded

243 fossil fuel emission dataset (GridFED; Jones et al., 2021). LBCO₂ tracers were simulated using
244 two sets of terrestrial biosphere fluxes from the Carnegie-Ames-Stanford Approach (CASA)
245 biogeochemical model (Randerson et al., 1997) and Vegetation Integrative Simulator for Trace
246 Gases (VISIT) (Ito, 2019).

247

248 **2.4.2 CarbonTracker (CT) inverse model**

249 To understand the temporal pattern of atmospheric CO₂ mole fraction over the study station
250 and the IGP region, we used simulated CO₂ mole fraction from an inverse modelling
251 framework CarbonTracker (CT) (Peters et al., 2005). Here, we used the CarbonTracker 2022
252 release (CT2022), which incorporated two-way nesting of the offline atmospheric tracer
253 transport model TM5, supporting coarse-resolution global data and high-resolution regional
254 data (Krol et al., 2004). The TM5 model in CT2022 was driven with meteorology from the
255 ERA-interim reanalysis provided by the European Center for Medium-Range Weather
256 Forecasts (ECMWF). The CT2022 inverse model simulated atmospheric CO₂ mole fraction by
257 correcting the prior specifications of CO₂ sources and sinks in the model by assimilating global
258 in situ observations. In this study, we used the CT2022-simulated CO₂ mole fraction from
259 February 2023 to October 2023.

260

261 **2.4.3 GEOS-Chem inverse model**

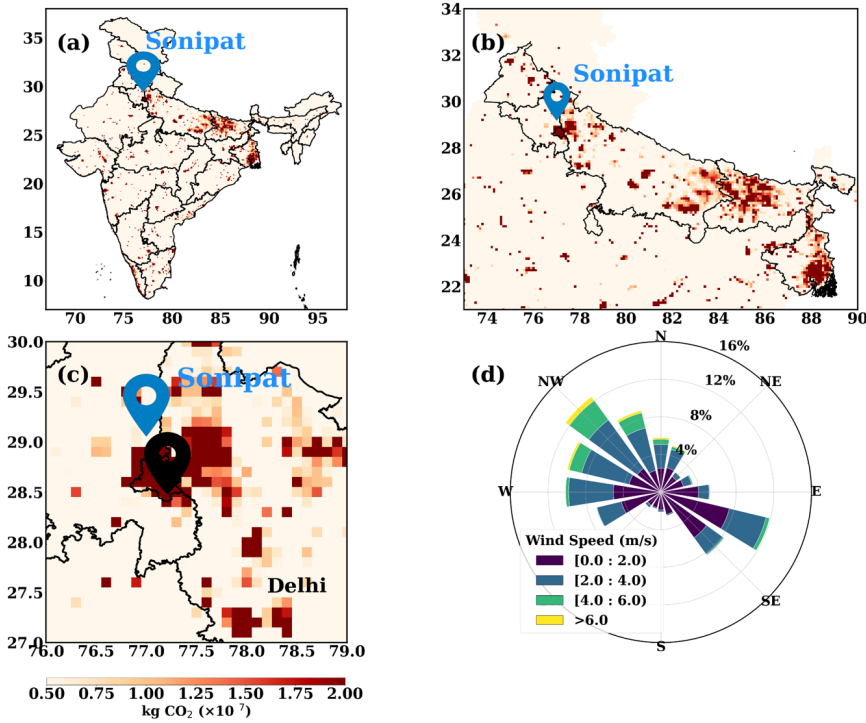
262 To study the seasonality of the fluxes over Sonipat, we used a four-dimensional variational
263 (4D-Var) assimilation system with the GEOS-Chem global chemical transport model
264 (CTM; Philip et al., 2019, 2022). The GEOS-Chem 4D-Var system was constrained with XCO₂
265 retrievals from the OCO-2 satellite (Philip et al., 2022), following the protocol of the OCO-2
266 v10 Multi-model Intercomparison Project (MIP) (Byrne et al., 2017; Liu et al., 2014). The Net
267 Ecosystem Exchange (NEE) fluxes for 2023 at a spatial resolution of 1° × 1°, constrained with
268 the OCO-2 Land Nadir and Land Glint observational modes are used here.

269

270 **2.4.4 Mi CASA terrestrial biospheric model**

271 We also used simulated CO₂ fluxes from a terrestrial biospheric model (TBM) in this study.
272 The Más informada Carnegie-Ames-Stanford-Approach (Mi CASA) model (Weir, 2024), a
273 comprehensive update to the CASA – Global Fire Emissions Database, version 3 (CASA-
274 GFED3) product, was utilised here (Chen et al., 2023; Potter et al., 1993). Mi CASA provides
275 daily global data at 0.1° resolution from January 2001 to December 2023. This includes carbon
276 flux variables from sources such as net primary production (NPP), heterotrophic respiration

277 (Rh), wildfire emissions (FIRE), and fuel wood burning emissions (FUEL). The model is
 278 driven with meteorological data from NASA's Modern-Era Retrospective analysis for Research
 279 and Application, Version 2 (MERRA-2).



280
 281 **Figure 1:** Anthropogenic CO₂ emissions over (a) India (b) IGP and (c) Sonipat/Delhi derived
 282 from the EDGAR emission inventory for 2021. (d) Annually averaged wind patterns over
 283 Sonipat for February 2023 – January 2024.

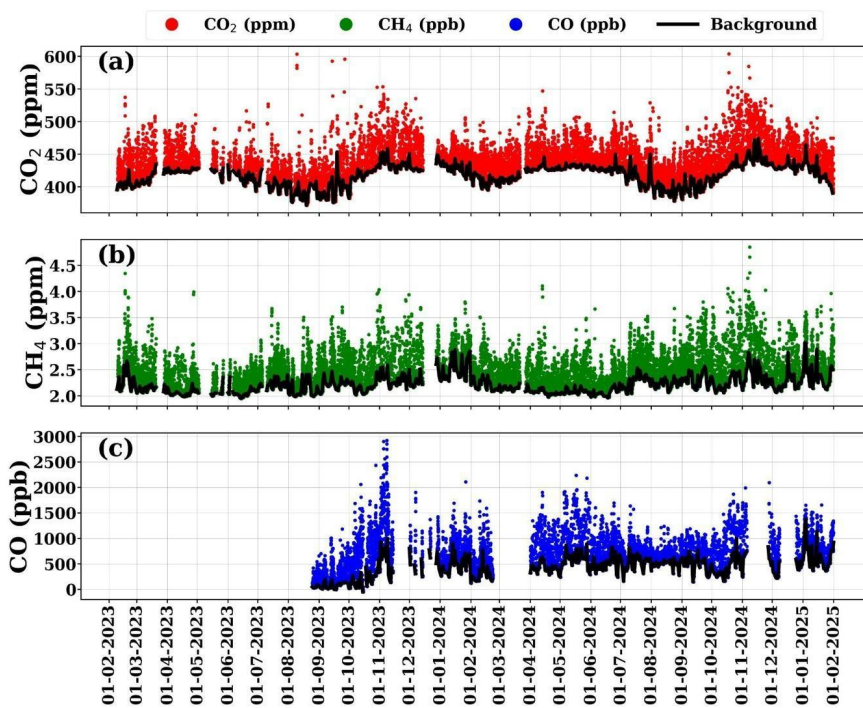
284
 285

286 3. Results and discussions

287 3.1 CO₂ measurements at Sonipat station

288 Figures 1(a-c) illustrate the annual mean anthropogenic CO₂ emissions over India, IGP and
 289 Delhi/Sonipat for 2021 based on the EDGAR emission inventory, a major hotspot of
 290 anthropogenic CO₂ emissions. The dominant wind direction over Sonipat was from the

291 northwest during the study period, highlighting influence from upwind sources of pollution and
 292 greenhouse gases (Figure 1d). Seasonal changes in meteorological parameters (air temperature,
 293 relative humidity, rainfall and wind; Figures S2 and S3) were also analysed alongside CO₂ to
 294 better understand the role of meteorology in Sonipat. In this study, we focus on seasonal and
 295 diurnal CO₂ variability and compare these patterns with those at other stations in India and in
 296 the same latitudinal band across the globe to uncover the unique aspects of CO₂ dynamics over
 297 Sonipat and the IGP.



298 **Figure 2:** (a) Hourly averaged time series of atmospheric (a) CO₂, (b) CH₄, and (c) CO mole
 299 fraction for the study period (February 2023 to January 2025) over Sonipat. The thick black
 300 line represents the background mole fraction estimated using the ADVS method. CO₂ and CH₄
 301 measurements were made using a Picarro GHG analyser, and CO measurements were made
 302 using CUPI-G sensor.

303
 304
 305 Figure 2 presents the hourly averaged time series of atmospheric (a) CO₂, (b) CH₄, and
 306 (c) CO mole fractions at Sonipat during the study period (February 2023 to January 2025).

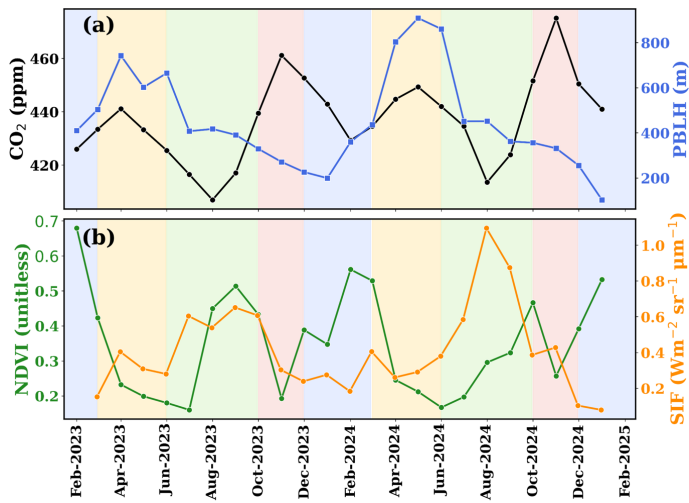
307 Hourly CO₂ mole fractions range from ~380 ppm to ~550 ppm, indicating strong monthly
308 variations in CO₂ mole fractions at the monitoring station. The lowest CO₂ mole fractions were
309 observed from July to August, which coincided with weak CO and strong CH₄ values. The
310 highest mole fractions of CO₂ were observed from October to November, coinciding with the
311 highest mole fractions of CO and CH₄. We found an annual mean CO₂ mole fraction of
312 440.8±19.7 ppm for 2024 and compared it with those from other monitoring stations across
313 India (Table S1). Interestingly, despite differences in site characteristics, the annual mean CO₂
314 levels at rural stations like Gadanki and urban stations like Ahmedabad are comparable,
315 whereas Sonipat shows distinctly higher values.

316 **3.2 Seasonal variability**

317 **3.2.1 Seasonality of in situ observations**

318 Figure 3 shows the monthly mean atmospheric CO₂ mole fractions during the study period. A
319 shaded background has been used to distinguish the seasonal regimes used in this study. The
320 monthly mean CO₂ mole fraction shows a maximum in November (post-monsoon season) and
321 a minimum in August (monsoon season) in both years. The observed seasonal mean of CO₂
322 during different seasons were 440.8±19.7 ppm (pre-monsoon), 422.6±23.3 ppm (monsoon),
323 456.4±30.8 ppm (post-monsoon), and 440.5±19.7 ppm (winter).

324 The seasonal change in CO₂ mole fractions over the monitoring station is governed by
325 the strength of emission sources, photosynthetic activity (biospheric fluxes), local meteorology
326 and atmospheric transport. The planetary boundary layer height (PBLH), which is determined
327 by local meteorology, strongly influences CO₂ mole fractions. PBL is the lowest layer within
328 the troposphere, where temperature and wind speed variations are integral in modulating its
329 height. During pre-monsoon, deep convection due to the well-developed PBLH from the
330 surface to the upper troposphere results in lower mole fractions of CO₂, while the weakly
331 developed PBLH in winter leads to higher CO₂ (Baker et al., 2012; Kar et al., 2004; Park et al.,
332 2009; Patra et al., 2011; Randel and Park, 2006).



333

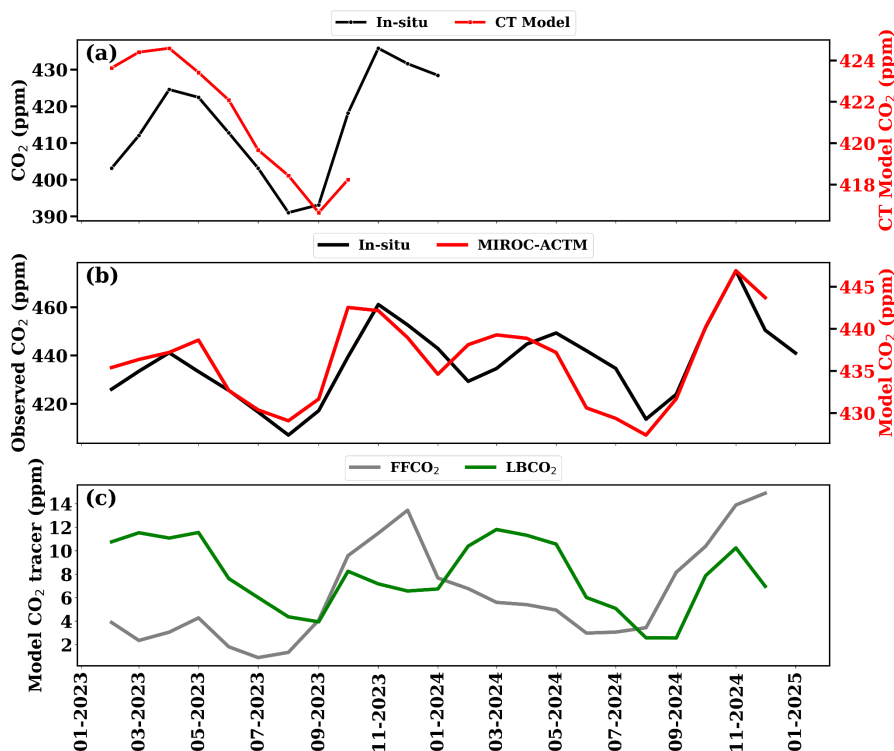
334 **Figure 3:** (a) Monthly variations of atmospheric CO₂ mole fraction (black) and PBLH (blue)
 335 and (b) NDVI (green) and SIF (orange) over the Sonipat monitoring station during the study
 336 period. The shaded background represents different seasons; yellow (pre-monsoon), green
 337 (monsoon), red (post-monsoon) and blue (winter).

338 The seasonal change in CO₂ was examined using two different vegetation indices
 339 (normalised difference vegetation index, NDVI and solar-induced fluorescence, SIF) to assess
 340 the role of the biosphere in CO₂ mole fractions over Sonipat. Both NDVI and SIF have been
 341 widely used as indicators of vegetation cover and photosynthetic activity (Aburas et al., 2015;
 342 Nath, 2014). Our analysis shows a strong inverse relationship between CO₂ levels and NDVI,
 343 as illustrated in Figure 3b. A noticeable decrease in atmospheric CO₂ mole fraction is observed
 344 at the onset of the monsoon (June), with increased vegetative activity continuing until
 345 September. Increased vegetation cover increases photosynthetic carbon uptake by the
 346 biosphere. However, as vegetation activity decreases from the post-monsoon to winter and pre-
 347 monsoon seasons, photosynthetic carbon uptake decreases, leading to a rise in atmospheric
 348 CO₂. Spearman's rank correlation analysis showed a weak and statistically insignificant
 349 relationship between CO₂ and NDVI ($\rho = -0.09$, $p = 0.74$). In contrast, CO₂ exhibited a
 350 moderate negative correlation with SIF ($\rho = -0.42$, $p = 0.07$). The negative correlation with
 351 SIF is consistent with enhanced biospheric uptake during periods of increased photosynthetic
 352 activity. Similar studies (Metya et al., 2021; Sreenivas et al., 2016; Tiwari et al., 2014), over
 353 India exhibited a strong dependence of CO₂ seasonality on local vegetative carbon uptake.

354 A sharp decrease in the seasonal mean (~18 ppm) was noted from pre-monsoon to
355 monsoon, attributed to enhanced photosynthetic activity around the measurement site, driven
356 by abundant soil moisture. A further decrease in CO₂ mole fraction is also observed as the
357 monsoon progresses, with minimum CO₂ mole fractions observed in August. The decreases in
358 temperature (due to cloudy, overcast conditions prevailing during these months) reduce leaf
359 and soil respiration, thereby enhancing carbon uptake (Jing et al., 2010; Patil et al., 2014).
360 Further, an increase in CO₂ mole fraction (~34 ppm) is observed during post-monsoon,
361 reflecting higher ecosystem respiration (Sharma et al., 2014) and enhanced soil microbial
362 activity (Fan & Forkel, 2025; Munksgaard et al., 2022), particularly from nocturnal respiration
363 prior to crop harvest. The gradual decline in NDVI during this period indicates reduced CO₂
364 uptake by vegetation. This season coincided with crop-burning episodes in northern India,
365 which significantly increased CO₂ mole fractions. A sharp decrease (~16 ppm) in the seasonal
366 mean during winter is evident compared to the post-monsoon. The shallow PBLH and winds
367 from western IGP that transport crop-burning residue contribute to the enhanced mole fraction
368 during winter. Table S2 compares the seasonal amplitude and the peak and drawdown months
369 at the measurement site with those in similar studies across India. Sonipat exhibits higher
370 seasonal amplitudes than other sites. However, a similar pattern in CO₂ peak and drawdown
371 months is evident in other monitoring stations.

372 3.2.2 Seasonal constraints from model and satellites

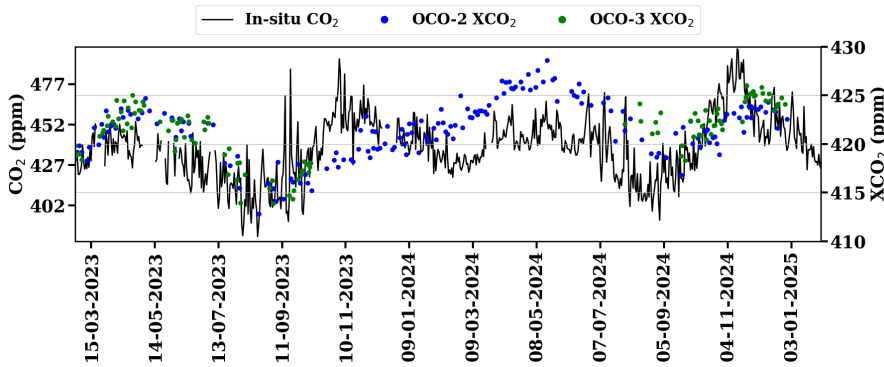
373 Figure 4(a) shows the comparison of ground-based mole fraction of CO₂ with CarbonTracker
374 inverse model (CT2022) simulated mole fraction (see different y-axis). The model outputs
375 beyond October 2023 were not publicly available. In general, the CT2022 model-simulated
376 mole fractions are much lower than the observed mole fractions at the Sonipat station. The
377 discrepancy is mainly due to the model's coarser resolution. Nevertheless, the model-simulated
378 seasonal pattern of CO₂ mole fraction is broadly in agreement with observations (Figure 4).
379 The CT2022 model simulates a minimum mole fraction of 416 ppm in September, whereas in
380 situ measurements show a minimum of 407 ppm in August. The CT2022 model exhibits higher
381 mole fractions during the pre-monsoon season, consistent with in situ data. Note that most
382 global and regional chemical transport models were unable to reproduce the large seasonal
383 amplitude of surface-based measured atmospheric CO₂ mole fractions at any of the monitoring
384 stations in India with different ecosystems (Lin et al., 2018; Philip et al., 2022).



385
 386 **Figure 4:** (a) Monthly mean background CO₂ mole fraction over Sonipat (estimated using the
 387 ADVS method) compared to CarbonTracker (CT2022) model-simulated values at daytime
 388 (13:00 – 16:00). Note that the left y-axis represents surface mole fraction from in situ
 389 measurements, and the right y-axis represents CT2022-simulated mole fraction. (b) comparison
 390 of simulated mole fraction of atmospheric CO₂ from MIROC-ACTM with in situ
 391 measurements at Sonipat and (c) monthly averaged time series of different tracers from the
 392 MIROC-ACTM.

393
 394 Figure 4(b) shows the comparison of atmospheric CO₂ mole fractions over Sonipat with
 395 the simulated mole fraction of CO₂ from the MIROC4-ACTM model. Similar to CT2022,
 396 MIROC captures the seasonal pattern of CO₂, but fails to capture the actual seasonal amplitude
 397 over Sonipat. Figure 4(c) presents the monthly averaged time series of model-simulated CO₂
 398 tracers. The fossil fuel tracer (FFCO₂) exhibits a peak in the post-monsoon period, followed by
 399 a gradual decrease through the end of winter. The shallow PBLH during this time traps
 400 vehicular emissions from NH-44 and industrial sources upwind of the monitoring station,

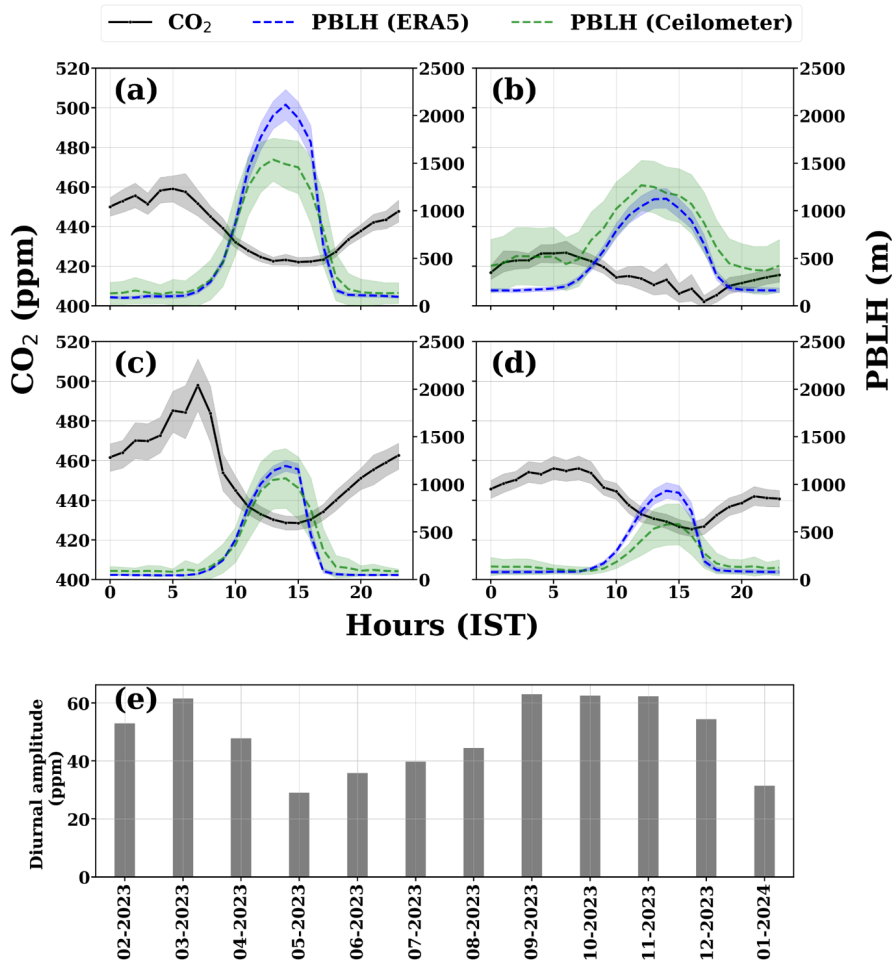
401 resulting in higher FFCO₂. With the development of the PBLH in the pre-monsoon, FFCO₂
 402 shows a gradual decrease, and rainfall during the monsoon results in minimum values during
 403 this time. The biospheric tracer (LBCO₂) shows a peak during the pre-monsoon, driven by dry
 404 soil conditions and a lack of vegetation and a drawdown during the monsoon. A sharp increase
 405 in LBCO₂ is observed during the post-monsoon season, coinciding with the harvest period at
 406 the monitoring station. Being surrounded by agricultural land, Sonipat is prone to emissions
 407 from crop residue burning around and upwind of the monitoring station. Both models
 408 underestimate these enhancements from regional sources.



409 **Figure 5:** Daily variations of atmospheric CO₂ mole fraction from in situ measurements over
 410 Sonipat (left y-axis) with column average CO₂ mole fraction (XCO₂) from the OCO-2 (ppm)
 411 and OCO-3 (ppm) satellite instruments (right y-axis).
 412
 413

414 Figure 5 compares XCO₂ from OCO-2 and OCO-3 satellites with ground-based CO₂
 415 measurements at Sonipat during the study period. XCO₂ reveals a similar seasonal pattern with
 416 high mole fraction during the pre-monsoon season, followed by a drawdown in CO₂ mole
 417 fraction during the monsoon season and a further gradual increase in CO₂ during the post-
 418 monsoon and winter. Although the satellite column data captures the monthly variability
 419 reasonably well, it fails to capture the sharp increase in mole fraction during the post-monsoon.
 420 This post-monsoon enhancement from crop residue burning at the monitoring station, along
 421 with additional transport from Punjab, highlights the limitations of high-resolution satellite data
 422 in capturing local enhancements.

Deleted: regional scale



424
 425 **Figure 6:** (a-d) Seasonally-averaged diurnal variation of atmospheric CO₂ over the Sonipat
 426 station during the pre-monsoon (MAM), monsoon (JJAS), post-monsoon (ON) and winter
 427 (DJF) seasons with planetary boundary layer heights (blue denotes PBLH from ERA5 and
 428 green denotes PBLH derived from Ceilometer), (e) monthly variation of the diurnal amplitude
 429 of CO₂ from February 2023 to January 2024.

430
 431 **3.3 Diurnal variability**

432 Figure 6 (a-d) presents the averaged diurnal variation of atmospheric CO₂ mole
 433 fractions along with PBLH from ERA5 and Ceilometer at Sonipat during four seasons for the

434 first year of the study (February 2023 – January 2024). Figure S5 presents the diurnal variation
435 for the second year of the study. The diurnal cycle has been analysed separately for each year,
436 combining available PBLH data. All seasons exhibit a similar diurnal pattern, with maximum
437 CO₂ mole fractions in the early morning hours (05:00 - 08:00 am) and minimum mole fractions
438 in the late afternoon hours (2:00 - 3:00 pm). The observed diurnal cycle of CO₂ is closely
439 associated with the development of PBLH during the day (Figure 6). The peak in CO₂ mole
440 fraction during the morning hours can be attributed to the fumigation effect, and a well-mixed
441 PBL dilutes CO₂ mole fractions during the afternoon hours.

Deleted: S4

442 Photosynthetic activity is another key driver of diurnal variability at Sonipat, a
443 characteristic observed in rural areas with vegetative cover (Imasu & Tanabe, 2018). Strong
444 vegetative uptake of CO₂ during the monsoon results in minimum daytime CO₂ mole fractions,
445 and the lack of vegetation during post-monsoon contributes to maximum daytime CO₂ mole
446 fractions during this season. The diurnal variation of GHGs reported by several studies
447 (Nishanth et al., 2014; Patil et al., 2014; Sharma et al., 2014) from different parts of the country
448 shows a similar trend. The same was observed for 2024 as well (Figure S5). The diurnal
449 variability of CO₂ over Sonipat is driven by biospheric activity and local meteorology.

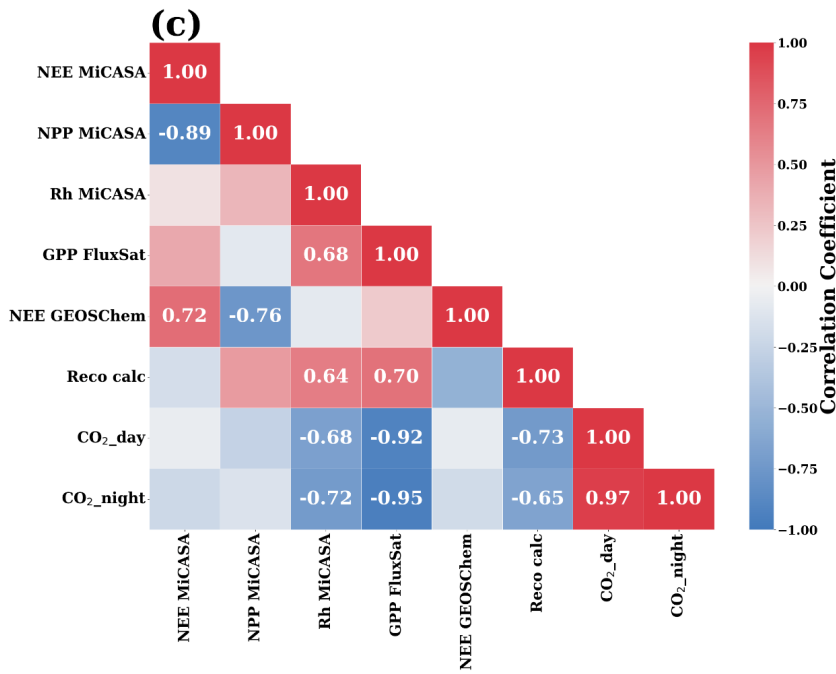
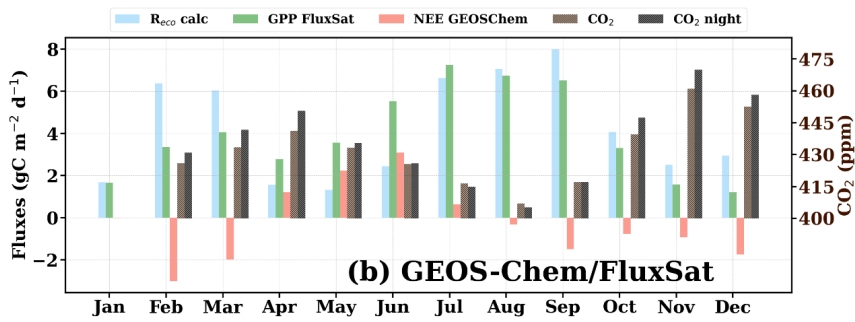
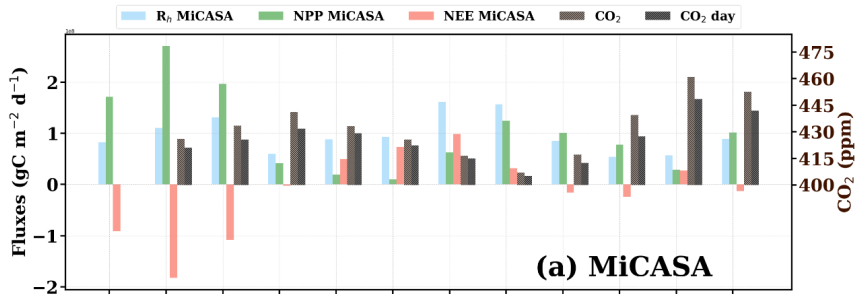
Deleted: S4

450 Figure 6(e) shows the monthly average variation in diurnal amplitude (difference between the
451 maximum and minimum mole fraction of CO₂ in the diurnal cycle) during the first year. The
452 lowest diurnal amplitude of about 29 ppm is observed in May, while the highest amplitude at
453 about 63 ppm is observed in September/October. We found that the post-monsoon season
454 exhibited the highest diurnal variability (~60 ppm), followed by the pre-monsoon (~35 ppm),
455 winter (~30 ppm), and monsoon (~20 ppm) seasons.

456

457 **3.4 Drivers of CO₂ seasonality**

458 The contribution of biospheric fluxes in driving the CO₂ mole fraction over Sonipat (for
459 2023) was analysed in Figure 7. Figure 7(a) shows the simulated data from the Mi CASA
460 biosphere model along with the monthly averaged mole fractions of CO₂ and daytime CO₂
461 (06:00 – 18:00). Figure 7(b) presents the simulated NEE from GEOS-Chem and GPP from
462 FluxSat, along with the monthly averaged mole fractions of daily-mean and nighttime CO₂
463 (18:00 – 06:00). Positive NEE values indicate a net exchange of CO₂ from the biosphere to the
464 atmosphere. On the other hand, a negative NEE value (when NPP exceeds Rh) suggests the
465 uptake of CO₂ from the atmosphere to the biosphere.



469 **Figure 7:** Monthly variation of atmospheric CO₂ mole fraction (for 2023) over the Sonipat
470 monitoring station compared against (a) biospheric fluxes from the MiCASA terrestrial
471 biospheric model and (b) GEOS-Chem model and FluxSat GPP data. (a - b) The CO₂ mole
472 fraction are daytime-mean (06:00 - 18:00 LT) and night time-mean (18:00 - 06:00 LT). The
473 correlation heatmap of all the variables. The annual growth rate of CO₂ has been subtracted
474 from the CO₂ mole fraction using background data from the Mauna Lou observatory. The
475 variable “Reco calc” was calculated as the difference between NEE (GEOS-Chem) and GPP
476 (FluxSat). The Pearson correlation coefficients with a p value less than 0.05 have been
477 displayed in the correlation plot.

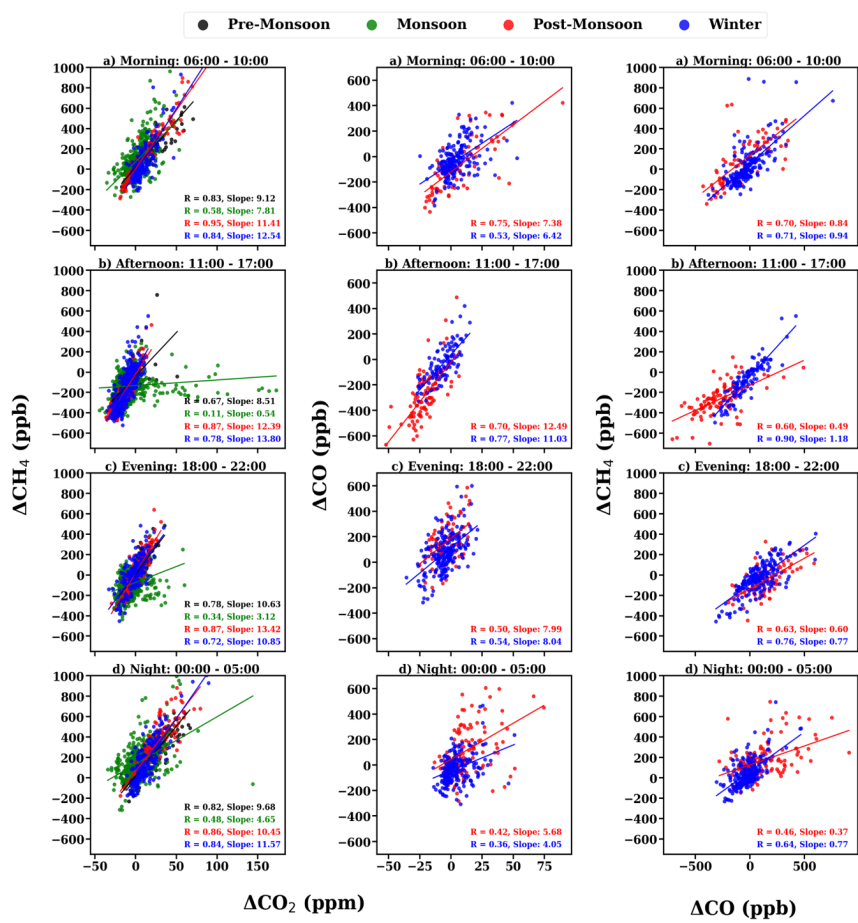
478

479 The NEE flux shows a strong positive in June, followed by a gradual decrease through
480 October (monsoon). During this time, Reco, Rh and GPP exhibit strong enhancements. These
481 enhancements are accompanied by a drawdown of CO₂ during this time. The driving factor
482 behind this CO₂ drawdown during monsoon is the enhanced ecosystem productivity during this
483 time. Strong inverse correlations of GPP, Rh, and Reco with CO₂ suggested that the biosphere
484 acts as a net sink of CO₂ (Figure 8c).

485 Interestingly, post-monsoon and winter months exhibit weak or negative NEE. This is
486 because Rh values are low during these seasons due to drier soil conditions and lower soil
487 moisture. It is also notable that GPP is very low during these months, which is associated with
488 a high CO₂ mole fraction. Significant contributions of air-mass transport from upwind regions
489 and boundary-layer dynamics, along with the lack of vegetation during this time, contribute to
490 the buildup of CO₂ mole fraction.

491

492



493
 494 **Figure 8:** Tracer-tracer relations of $\Delta\text{CO}_2/\Delta\text{CH}_4$ (left panel), $\Delta\text{CO}_2/\Delta\text{CO}$ (middle panel) and
 495 $\Delta\text{CH}_4/\Delta\text{CO}$ (right panel) during a) Morning (0600–1000 IST), b) afternoon (1100–1700 IST),
 496 c) evening (1800–2200 IST) and d) night (0000–0500 IST).

497
 498 **3.5 Emission source detection using tracer-tracer relationships**

499 The ratios (tracer-tracer) of GHGs have been widely used in previous studies to estimate
 500 different emission source contributions to atmospheric GHGs (Chandra et al., 2016, 2019; Lin
 501 et al., 2015; Lopez, 2012; Paris et al., 2008; Sreenivas et al., 2016, 2022). We followed a similar
 502 tracer-tracer correlation analysis to assess synoptic variation in CO_2 across different diurnal
 503 time windows and understand the emission sources contributing to CO_2 mole fractions over

504 Sonipat (Figure 8). The measurements have been divided into four-time windows: (a) morning
505 hours (06:00 - 10:00; the PBLH starts to develop after sunrise; local traffic is high), (b)
506 afternoon hours (11:00 - 17:00; the PBLH is well-developed; relatively minimum local traffic,
507 (c) evening hours (18:00 - 22:00; rush hour traffic and high household emissions), and (d) night
508 hours (00:00 - 00:05; relatively less anthropogenic emission sources). Excess mole fractions
509 were used in the correlation analysis to remove the influence of background mole fractions on
510 the correlation ratios (Worthy et al., 2009). The correlation between the different gases (CO₂,
511 CH₄, and CO) has been studied using the robust linear fit regression method.

512

513 Figure 8 (left panel) presents the correlation of excess mole fraction of CH₄ and CO₂
514 during the four seasons. The CH₄/CO₂ correlation reveals a strong correlation ($r > 0.6$) for all
515 seasons except monsoon during all time windows, which suggests a similar source mechanism
516 or a controlling emission process for both gases at the measurement site. Around the monitoring
517 station, vehicular emissions from the nearby highway and natural gas combustion emissions
518 are possible sources. Also, a positive correlation suggests that anthropogenic emissions
519 dominate the carbon cycle in Sonipat (Fang et al., 2015). The regression slope shows strong
520 diurnal variation throughout all seasons. Recent studies across India have reported similar
521 results, with higher regression slopes during the post-monsoon and winter seasons than during
522 the pre-monsoon and monsoon seasons (Lin et al., 2015; Sreenivas et al., 2016, 2022).

523

524 Figure 8 (middle panel) presents the correlation of excess mole fractions of CO and
525 CO₂ during post-monsoon and winter. The CO/CO₂ ratio over Sonipat (4 – 12.5 ppb ppm⁻¹) is
526 lower than that for fresh plumes from wildfire (Andreae and Merlet, 2001; Mauzerall et al.,
527 1998) and much lower than that from biomass burning events alone (Matsueda et al., 1999).
528 Lin et al. (2015) reported CO/CO₂ ratios of 13 ppb ppm⁻¹ over Southeast Asian outflow from
529 February to April 2001. This value was found to be influenced by fossil fuel emissions (Russo
530 et al., 2003), crop residue burning, and biofuel burning rather than solely by biomass/biofuel
531 burning. The CO/CO₂ ratios over Sonipat during the post-monsoon and winter closely match
532 those of Lin et al. (2015), suggesting that the high CO₂ mole fractions during this time are an
533 interplay of different sources like crop residue burning (long-range transport) and other fossil-
534 fuel emissions (vehicular and industrial) around the monitoring station.

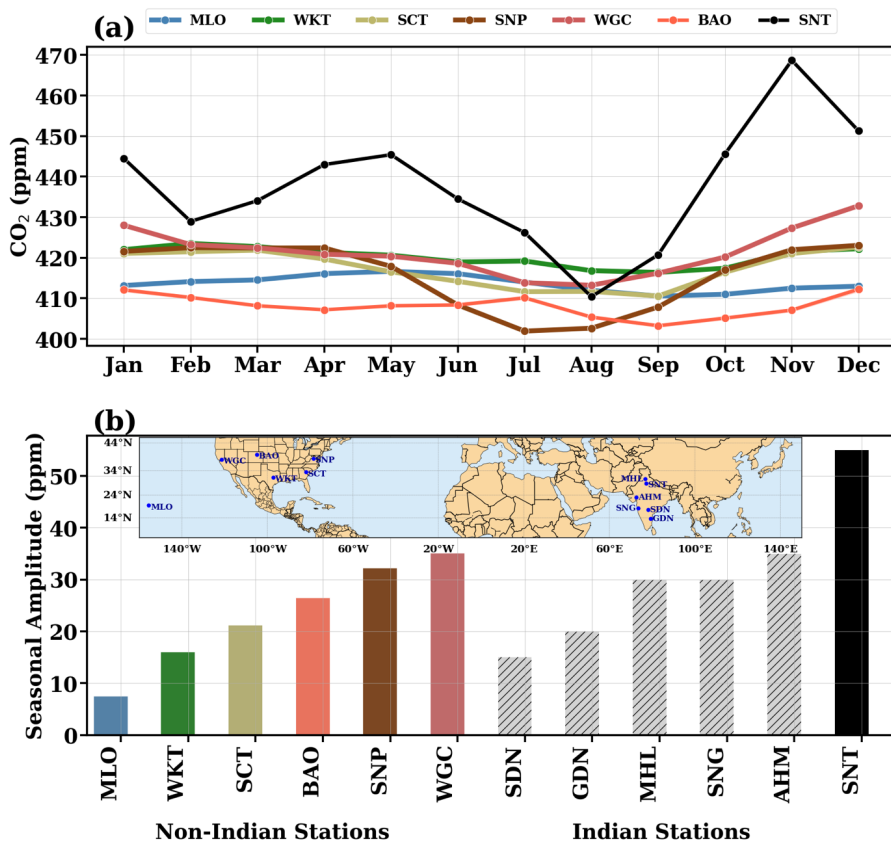
535

536 Figure 8 (right panel) presents the correlation of excess mole fractions of CH₄ and CO during
537 post-monsoon and winter. The CH₄/CO ratios range from 0.3 to 1.2 at Sonipat, indicative of

538 anthropogenic emission sources (Bakwin et al., 1995; Harriss et al., 1994; Lai et al., 2010; Lin
 539 et al., 2015; Niwa et al., 2012; Sawa et al., 2004; Wada et al., 2011; Xiao et al., 2004). In
 540 contrast, ratios influenced solely by biomass and biofuel burning are much lower, ranging from
 541 0.07 to 0.3 (Andreae and Merlet, 2001; Mauzerall et al., 1998; Mühle et al., 2002).

542 These lower ratios highlight the significant difference when compared to the values
 543 recorded in Sonipat. Moreover, very high CH₄ emissions from livestock can elevate the
 544 generally low CH₄/CO ratios associated with biomass burning. This indicates substantial
 545 contributions from various CH₄ sources apart from biofuel burning.

546



547 **Figure 9:** (a) Comparison of the seasonal variability of atmospheric CO₂ over Sonipat
 548 monitoring station with various locations in the same latitudinal band. (b) Comparison of the
 549 seasonal amplitude between Indian (coloured bars) and international monitoring stations (grey
 550 bars). Indian stations include Shadnagar (SDN), Sinhadag (SNG), Ahmedabad (AHM), Mohali
 551 bars).

552 (MHL), Gadanki (GDN), and Sonipat (SNT). International stations include Mauna Loa (MLO),
553 South Carolina (SCT), Shenandoah National Park (SNP), Walnut Grove, (WGC), Moody
554 (WKT) and Boulder (BAO). For all international stations except BAO, the five-year average
555 (2018 - 2022) has been chosen for the seasonality. For BAO, 2011 – 2016 has been used due
556 to lack of coinciding data. The monthly average of the entire study period (February 2023 –
557 January 2025) has been used for this comparison.

558

559 4. Discussions

560 By investigating two years of high-frequency atmospheric CO₂ mole fraction measurements at
561 the Sonipat station in the IGP region, we identified the following salient features about the
562 seasonality, diurnal variability, drivers of temporal variability, and emission sources of CO₂.

563 **Very high atmospheric CO₂ mole fractions over IGP:** The surface-based
564 measurements of atmospheric CO₂ mole fraction exhibit strong seasonality, with a maximum
565 (456.4 ppm) during post-monsoon and a minimum (407.2 ppm) during monsoon, with an
566 average of 422.6 ppm. Seasonal changes in the PBLH affected the atmospheric CO₂ mole
567 fraction by diluting or concentrating GHG mole fractions near the surface. A strong dependence
568 of CO₂ seasonality on local vegetative carbon uptake was observed from the negative
569 correlation between NDVI and CO₂ mole fractions, which was consistent across India (Metya
570 et al., 2021; Sreenivas et al., 2016; Tiwari et al., 2014).

571 A comparison of the seasonality of atmospheric CO₂ at Sonipat with other Indian and
572 global sites in the same latitudinal band revealed very high seasonality at Sonipat, surpassing
573 that of all other stations. This high seasonality is attributed to elevated CO₂ mole fractions in
574 November (post-monsoon), driven by local emissions and crop residue burning. Figure 9a
575 presents the monthly averaged variation of CO₂ over Sonipat during the study period (SNT)
576 with other measurement sites in the same latitudinal band (5° N – 40° N). Details of all
577 monitoring stations used in this study are described in detail in S1. Sonipat exhibits a very high
578 seasonal amplitude (~60 ppm) compared to other sites worldwide (~15 ppm, see Figure 9b),
579 attributed to the sharp increase in post-monsoon, consistent in both years of the study (see
580 Figure 2). Excluding November would reduce the seasonal amplitude of Sonipat to 35 ppm,
581 which is comparable to that in Ahmedabad (35 ppm). Temperature-driven PBLH (which
582 inhibits mixing) and strong north-westerly winds (which induce transport of emissions from
583 upwind) during this season play a key role in these high CO₂ mole fractions (Figure S3 and

Deleted: S2

585 ~~S4~~. It is also noted that the CO₂ drawdown in August is primarily due to the green paddy fields
586 during the monsoon (terrestrial CO₂ uptake), coinciding with heavy rains that wash out CO₂.
587 This combined effect makes the lowest CO₂ mole fractions in Sonipat comparable to those at
588 some background stations across the globe with different ecosystems (Figure 9a).

Deleted: S3

589 This study also analysed the drivers of this variability using various ecosystem variables,
590 including NEE, which represents the net carbon exchange between terrestrial ecosystems (the
591 difference between Rh and NPP). NPP is the net amount of CO₂ retained in the biosphere. Rh
592 is the amount of CO₂ emitted into the atmosphere due to the decomposition of organic matter
593 by microorganisms in the soil. Reco, the sum of Ra (autotrophic respiration) and Rh has been
594 calculated as the difference of FluxSat GPP and GEOS-Chem NEE. GPP, a measure of carbon
595 uptake by plants, was observed to be very high during monsoon along with NEE, Rh and Reco.
596 Statistical analysis revealed a strong negative correlation of GPP with CO₂ and a strong positive
597 correlation with Rh and Reco. These suggest that the primary sink of CO₂ over Sonipat is
598 biospheric activity, driven by the abundance of vegetation resulting from enhanced soil
599 moisture during the monsoon.

600 **Performance of models and satellites over IGP:** Although both the CarbonTracker
601 and MIROC-ACTM models captured the broad seasonal pattern of CO₂ mole fractions, they
602 substantially underestimated it. However, MIROC showed greater seasonal variability than
603 CT2022, with post-monsoon highs and pre-monsoon drawdowns showing strong correlations
604 with in situ measurements. Further analysis of the tracers from MIROC provides insights into
605 the driving factors of this variability. The post-monsoon peak is attributed to vehicular
606 emissions from the nearby highway and industrial sources upwind of the monitoring station.
607 The drawdown in monsoon is attributed to the added soil moisture and increased CO₂ uptake
608 by plants during this time. The location of the measurement site in IGP, downwind of Punjab,
609 provides insights into this transport-induced enhancement. The OCO-2 and OCO-3 satellite
610 XCO₂ retrievals also showed similar seasonal variability; however, the satellites could not
611 capture CO₂ enhancements from local sources.

612 **Diurnal variability driven by meteorology:** The atmospheric CO₂ mole fraction at
613 Sonipat exhibits a consistent diurnal pattern across seasons. It was observed that CO₂ mole
614 fractions steadily increased throughout the night, reaching a peak in the early morning hours.
615 This accumulation of CO₂ during the night-time can be attributed to the fumigation effect: a
616 significant rise in surface mole fractions, notable during the early morning hours due to the

618 breakdown of the nocturnal inversion layer following sunrise (Stull, 1988). Weak winds and
619 shallow PBLH enhance the fumigation effect. The combined effect of photosynthetic activity
620 and mixing of PBLH during the afternoon hours drives the CO₂ mole fractions during different
621 seasons. The diurnal amplitude shows large month-to-month variation with an increasing trend
622 from May to September 2023 and a decreasing trend till February 2024. Figure S6 presents the
623 seasonal variation of CO₂ compared with PBLH derived from Ceilometer and ERA5 reanalysis
624 data for 2023. A slight shift in the timing of the morning peaks was observed from season to
625 season, due to changes in sunrise time, which affected photosynthetic activity.

Deleted: S5

626 **Detecting emission source contributions:** Tracer-tracer relationships across different
627 time periods during the post-monsoon and winter seasons were examined. Analysis reveals
628 that CO₂ and CH₄ exhibit a strong positive correlation across all seasons, suggesting common
629 sources for both gases. During monsoon season, the afternoon time window shows a weak
630 correlation with other time windows, revealing distinct source and sink mechanisms for CO₂
631 and CH₄, such as CH₄ loss via hydroxyl radical and CO₂ uptake by plants. The regression
632 slope is higher during the post-monsoon and winter months, when reduced photosynthetic
633 activity and the dominance of local emissions and long-range transport are observed. The
634 lower values during pre-monsoon and monsoon are associated with the dominance of
635 vegetation and terrestrial uptake of CO₂ by photosynthetic activity.

636 The CO/CO₂ correlation shows strong diurnal variability, suggesting the dominance of
637 different source mechanisms throughout the day, with strong correlation during the morning
638 and afternoon hours (suggesting a similar source) and weaker correlation during the evening
639 and night hours (suggesting different sources). The post-monsoon season shows higher
640 regression slopes due to reduced photosynthetic activity. Over Sonipat, the contribution of CO
641 and CO₂ from long-range air mass transport (influenced by crop residue burning in Punjab)
642 during post-monsoon from the northwest of the monitoring station is diluted by other sources
643 (such as vehicular emissions from highways, crop residue burning, and open burning). The
644 contribution of biofuel burning (which has a higher burning efficiency) during post-monsoon
645 and winter (Andreae and Merlet, 2001) can also reduce the CO/CO₂ ratios. Figure S4 presents
646 the wind patterns during the different seasons, revealing the predominant winds from the
647 northwest during the post-monsoon season. The CO/CO₂ ratios reveal the combined influence
648 of various sources around and upwind of the monitoring station during the post-monsoon
649 period.

Deleted: S2

652 The CH₄/CO correlation ($r > 0.7$) was stronger during winter than during post-monsoon
653 across all time windows, suggesting similar sources during winter and different sources during
654 post-monsoon. The regression slope was higher during winter than during the post-monsoon
655 period. This was traced to the lack of photosynthetic activity and the dominance of local
656 emissions and long-range transport. Lin et al. (2015) reported comparable CH₄/CO ratios at
657 Pondicherry (PON) and Port Blair (PBL). CH₄ and CO emissions from biomass, biofuel
658 burning and livestock estimated from EDGAR v4.2, 2011 indicate a CH₄/CO ratio of 0.64 –
659 0.69 over the Indian subcontinent from 2000-2008. These ratios are comparable to those
660 observed during both seasons at Sonipat.

661 In summary, this study demonstrated that this high temporal CO₂ variability across the
662 IGP region arises from an interplay of local anthropogenic and biomass-burning emissions,
663 biospheric fluxes, and prevailing meteorology.

664

665 **5. Conclusions**

666 In this study, we conducted high frequency measurements of atmospheric CO₂ mole fractions
667 at a suburban station in the Indo-Gangetic Plain, Sonipat and investigated the carbon cycle
668 dynamics over IGP. The atmospheric CO₂ mole fractions from February 2023 to January 2025
669 have been measured using a GHG analyser with laser-based cavity ring-down spectroscopy.
670 CO₂ molefractions over Sonipat recorded an annual average of 440.8±19.7 parts per million
671 (ppm) in 2024, with a very high seasonal variability of ~60 ppm, much higher than that of other
672 monitoring stations in the same latitudnal band. Post-monsoon recorded the highest diurnal
673 variability (~ 60 ppm) and monsoon recorded the least (~20 ppm) with a consistent diurnal
674 pattern irrespective of season. By examining a series of observational and modelling data, such
675 as ground-based and satellite-based measurements, three model outputs, ecosystem proxy
676 variables, and the tracer-tracer analysis technique, we identified the drivers of the high temporal
677 variability of CO₂ over Sonipat and the IGP region. First, this high seasonality is attributed to
678 elevated CO₂ mole fractions in November (post-monsoon), driven by local emissions and crop
679 residue burning. We found that biospheric activity was the primary driver of seasonal changes
680 over Sonipat, with anthropogenic emissions and soil respiration as the major sources and
681 photosynthetic carbon uptake as the major sink. In addition, boundary-layer dynamics and air-
682 mass transport from upwind regions significantly contribute to the buildup of CO₂ mole
683 fraction. Second, we found that although both the CarbonTracker and MIROC-ACTM models
684 captured the broad seasonal pattern of CO₂ mole fractions, they substantially underestimated
685 it. Moreover, the OCO-2 and OCO-3 satellite XCO₂ retrievals also showed similar seasonal

686 variability; however, the satellites could not capture CO₂ enhancements from local sources.
687 Third, we found that the atmospheric CO₂ mole fraction at Sonipat exhibits a consistent diurnal
688 pattern irrespective of season, with a maximum during the morning hours, attributed to the
689 fumigation effect, followed by a gradual decrease during the day and a minimum during the
690 afternoon hours, when photosynthetic activity is enhanced. Finally, tracer-tracer relationships
691 across different time periods in the post-monsoon and winter seasons revealed common sources
692 of CO₂ and CH₄. The CO/CO₂ ratios reveal the combined influence of vehicular emissions,
693 crop residue burning, and open burning on CO₂ mole fractions in Sonipat during the post-
694 monsoon period. This study identified key sources and drivers of the high CO₂ temporal
695 variability in a data-sparse IGP region. These findings advance our understanding of carbon
696 cycle dynamics, with direct implications for mitigation and policy.

697 **Data availability**

- 698 ● [The observational datasets used in this study are publicly available in a Zenodo](https://zenodo.org/record/19628722)
699 [archive and can be accessed from 10.5281/zenodo.19628722](https://zenodo.org/record/19628722)
- 700 ● The OCO-2 and OCO-3 data is downloaded from <https://disc.gsfc.nasa.gov/datasets/>.
701 This study utilizes the bias-corrected OCO-2 v11.1r data product
702 ([https://disc.gsfc.nasa.gov/datasets/OCO2_L2_Lite_FP_11.1r/summary?keywords=oco](https://disc.gsfc.nasa.gov/datasets/OCO2_L2_Lite_FP_11.1r/summary?keywords=oco2)
703 [2](https://disc.gsfc.nasa.gov/datasets/OCO2_L2_Lite_FP_11.1r/summary?keywords=oco2)) and the OCO-3 v10.4r data product
704 ([https://disc.gsfc.nasa.gov/datasets/OCO3_L2_Lite_FP_10.4r/summary?keywords=oco](https://disc.gsfc.nasa.gov/datasets/OCO3_L2_Lite_FP_10.4r/summary?keywords=oco3)
705 [3](https://disc.gsfc.nasa.gov/datasets/OCO3_L2_Lite_FP_10.4r/summary?keywords=oco3)).
- 706 ● The CT-2020 model outputs were downloaded from
707 <https://gml.noaa.gov/aftp/products/carbontracker/co2/>. The CASA model outputs
708 were downloaded from
709 [https://disc.gsfc.nasa.gov/datasets/GEOS_CASAGFED_M_FLUX_3/summary?keyw](https://disc.gsfc.nasa.gov/datasets/GEOS_CASAGFED_M_FLUX_3/summary?keywords=CASA)
710 [ords=CASA](https://disc.gsfc.nasa.gov/datasets/GEOS_CASAGFED_M_FLUX_3/summary?keywords=CASA).
- 711 ● The ERA5 reanalysis datasets were downloaded from
712 <https://cds.climate.copernicus.eu/cdsapp#!/dataset/reanalysis-era5-single-levels>.
- 713 ● The satellite estimates of NDVI were downloaded from
714 <https://www.ncei.noaa.gov/data/land-normalized-difference-vegetation-index/access/>.
- 715 ● This study utilises bias-corrected SIF data from OCO-2 v11r data product
716 ([https://disc.gsfc.nasa.gov/datasets/OCO2_L2_Lite_SIF_11r/summary?keywords=oco](https://disc.gsfc.nasa.gov/datasets/OCO2_L2_Lite_SIF_11r/summary?keywords=oco2%20sif)
717 [2%20sif](https://disc.gsfc.nasa.gov/datasets/OCO2_L2_Lite_SIF_11r/summary?keywords=oco2%20sif)).

- 718 • The FluxSat data is downloaded from
719 https://avdc.gsfc.nasa.gov/pub/tmp/FluxSat_GPP/. This study uses FluxSat version
720 2.2 dataproduct.
721 • The ObsPack data is available at <https://gml.noaa.gov/ccgg/obspack/data.php>. This
722 study used ObsPack V2.0 dataproduct.
723

724

Acknowledgements:

725 We acknowledge institutional support and funding provided by IIT Delhi and other
726 stakeholders to develop the IIT Delhi Atmospheric Observatory at Sonipat. In particular, we
727 thank Shahzad Gani (IIT Delhi) for his contribution to the observatory. We thank the Aakash
728 Project team for providing trace gas data from the CUPI-G sensors. We acknowledge the OCO-
729 2, OCO-3, CASA, CarbonTracker, and ERA5 teams for providing the data used in this study.
730

731

732

Author Contributions:

733 **Conceptualization:** VJV, RKK, SP

734 **Data curation:** VJV, RKK, JR, DG, SD, [TN](#), YM, PKP

735 **Investigation, Methodology:** VJV, RKK, SP, PKP

736 **Software, Visualisation:** VJV

737 **Writing – original draft:** VJV

738 **Writing – review & editing:** RKK, SP, JR, DG, SD, YM, PKP

739

Competing interests

741 The authors declare that they have no conflict of interest.

742 **References**

- 743 Aburas, M. M., Abdullah, S. H., Ramli, M. F., and Ash'aari, Z. H.: Measuring Land Cover
744 Change in Seremban, Malaysia Using NDVI Index, *Procedia Environmental Sciences*, 30,
745 238–243, <https://doi.org/10.1016/j.proenv.2015.10.043>, 2015.
- 746 Ammoura, L., Xueref-Remy, I., Gros, V., Baudic, A., Bonsang, B., Petit, J.-E., Perrussel, O.,
747 Bonnaire, N., Sciare, J., and Chevallier, F.: Atmospheric measurements of ratios between
748 CO₂ and co-emitted species from traffic: a tunnel study in the Paris
749 megacity, *Atmos. Chem. Phys.*, 14, 12871–12882, [https://doi.org/10.5194/acp-14-12871-](https://doi.org/10.5194/acp-14-12871-2014)
750 2014, 2014.
- 751 Andreae, M. O. and Merlet, P.: Emission of trace gases and aerosols from biomass burning,
752 *Global Biogeochemical Cycles*, 15, 955–966, <https://doi.org/10.1029/2000GB001382>, 2001.
- 753 Apadula, F., Cassardo, C., Ferrarese, S., Heltai, D., and Lanza, A.: Thirty Years of
754 Atmospheric CO₂ Observations at the Plateau Rosa Station, Italy, *Atmosphere*, 10, 418,
755 <https://doi.org/10.3390/atmos10070418>, 2019.
- 756 Baars, H., Ansmann, A., Engelmann, R., and Althausen, D.: Continuous monitoring of the
757 boundary-layer top with lidar, *Atmospheric Chemistry and Physics*, 8, 7281–7296,
758 <https://doi.org/10.5194/acp-8-7281-2008>, 2008.
- 759 Baker, A. K., Schuck, T. J., Brenninkmeijer, C. A. M., Rauthe-Schöch, A., Slemr, F., van
760 Velthoven, P. F. J., and Lelieveld, J.: Estimating the contribution of monsoon-related
761 biogenic production to methane emissions from South Asia using CARIBIC observations,
762 *Geophysical Research Letters*, 39, <https://doi.org/10.1029/2012GL051756>, 2012.
- 763 Bakwin, P. S., Tans, P. S., Zhao, C., Ussler III, W., and Quesnell, E.: Measurements of
764 carbon dioxide on a very tall tower, *Tellus B: Chemical and Physical Meteorology*, 47, 535–
765 549, <https://doi.org/10.3402/tellusb.v47i5.16070>, 1995.
- 766 Bhattacharya, S. K., Borole, D. V., Francy, R. J., Allison, C. E., Steele, L. P., Krummel, P.,
767 Langenfelds, R., Masarie, K. A., Tiwari, Y. K., and Patra, P. K.: Trace gases and CO₂ isotope
768 records from Cabo de Rama, India, *Current Science*, 97, 1336–1344, 2009.
- 769 Bisht, J. S. H., Machida, T., Chandra, N., Tsuboi, K., Patra, P. K., Umezawa, T., Niwa, Y.,
770 Sawa, Y., Morimoto, S., Nakazawa, T., Saitoh, N., and Takigawa, M.: Seasonal Variations of
771 SF₆, CO₂, CH₄, and N₂O in the UT/LS Region due to Emissions, Transport, and Chemistry,
772 *JGR Atmospheres*, 126, e2020JD033541, <https://doi.org/10.1029/2020JD033541>, 2021.
- 773 Brad Weir (2024), MiCASA Daily NPP Rh Fire Fuel Fluxes 0.1 degree × 0.1 degree V1,
774 Greenbelt, MD, USA, NASA Center for Climate Simulation (NCCS) DataPortal, Accessed:
775 [March 20, 2025], 10.5067/ZBXSA1LEN453
- 776 Byrne, B., Jones, D. B. A., Strong, K., Zeng, Z. -C., Deng, F., and Liu, J.: Sensitivity of CO₂
777 surface flux constraints to observational coverage, *JGR Atmospheres*, 122, 6672–6694,
778 <https://doi.org/10.1002/2016JD026164>, 2017.
- 779 Chakraborty, S., Tiwari, Y. K., Deb Burman, P. K., Baidya Roy, S., and Valsala, V.:
780 Observations and Modeling of GHG Concentrations and Fluxes Over India, in: Assessment

781 of Climate Change over the Indian Region: A Report of the Ministry of Earth Sciences
782 (MoES), Government of India, edited by: Krishnan, R., Sanjay, J., Gnanaseelan, C.,
783 Mujumdar, M., Kulkarni, A., and Chakraborty, S., Springer, Singapore, 73–92,
784 https://doi.org/10.1007/978-981-15-4327-2_4, 2020.

785 Chandra, N., Lal, S., Venkataramani, S., Patra, P. K., and Sheel, V.: Temporal variations of
786 atmospheric CO₂ and CO at Ahmedabad in western India, *Atmos.*
787 *Chem. Phys.*, 16, 6153–6173, <https://doi.org/10.5194/acp-16-6153-2016>, 2016.

788 Chandra, N., Venkataramani, S., Lal, S., Patra, P. K., Ramonet, M., Lin, X., and Sharma, S.
789 K.: Observational evidence of high methane emissions over a city in western India,
790 *Atmospheric Environment*, 202, 41–52, <https://doi.org/10.1016/j.atmosenv.2019.01.007>,
791 2019.

792 Chandra, N., Patra, P. K., Bisht, J. S. H., Ito, A., Umezawa, T., Saigusa, N., Morimoto, S.,
793 Aoki, S., Janssens-Maenhout, G., Fujita, R., Takigawa, M., Watanabe, S., Saitoh, N., and
794 Canadell, J. G.: Emissions from the Oil and Gas Sectors, Coal Mining and Ruminant Farming
795 Drive Methane Growth over the Past Three Decades, *Journal of the Meteorological Society*
796 *of Japan*, 99, 309–337, <https://doi.org/10.2151/jmsj.2021-015>, 2021.

797 Chandra, N., Patra, P. K., Niwa, Y., Ito, A., Iida, Y., Goto, D., Morimoto, S., Kondo, M.,
798 Takigawa, M., Hajima, T., and Watanabe, M.: Estimated regional CO₂ flux and uncertainty
799 based on an ensemble of atmospheric CO₂ inversions, *Atmos. Chem. Phys.*, 22, 9215–9243,
800 <https://doi.org/10.5194/acp-22-9215-2022>, 2022.

801 Chen, H., Karion, A., Rella, C. W., Winderlich, J., Gerbig, C., Filges, A., Newberger, T.,
802 Sweeney, C., and Tans, P. P.: Accurate measurements of carbon monoxide in humid air using
803 the cavity ring-down spectroscopy (CRDS) technique, *Atmospheric Measurement*
804 *Techniques*, 6, 1031–1040, <https://doi.org/10.5194/amt-6-1031-2013>, 2013.

805 Chen, Y., Hall, J., Van Wees, D., Andela, N., Hantson, S., Giglio, L., Van Der Werf, G. R.,
806 Morton, D. C., and Randerson, J. T.: Multi-decadal trends and variability in burned area from
807 the fifth version of the Global Fire Emissions Database (GFED5), *Earth Syst. Sci. Data*, 15,
808 5227–5259, <https://doi.org/10.5194/essd-15-5227-2023>, 2023.

809 Crisp, D., Pollock, H. R., Rosenberg, R., Chapsky, L., Lee, R. A. M., Oyafuso, F. A.,
810 Frankenberg, C., O'Dell, C. W., Bruegge, C. J., Doran, G. B., Eldering, A., Fisher, B. M., Fu,
811 D., Gunson, M. R., Mandrake, L., Osterman, G. B., Schwandner, F. M., Sun, K., Taylor, T.
812 E., Wennberg, P. O., and Wunch, D.: The on-orbit performance of the Orbiting Carbon
813 Observatory-2 (OCO-2) instrument and its radiometrically calibrated products, *Atmos. Meas.*
814 *Tech.*, 10, 59–81, <https://doi.org/10.5194/amt-10-59-2017>, 2017.

815 Das, C., Kunchala, R. K., Chandra, N., Chhabra, A., and Pandya, M. R.: Characterizing the
816 regional XCO₂ variability and its association with ENSO over India inferred from GOSAT
817 and OCO-2 satellite observations, *Science of The Total Environment*, 902, 166176,
818 <https://doi.org/10.1016/j.scitotenv.2023.166176>, 2023.

819 Eldering, A., O'Dell, C. W., Wennberg, P. O., Crisp, D., Gunson, M. R., Viatte, C., Avis, C.,
820 Braverman, A., Castano, R., Chang, A., Chapsky, L., Cheng, C., Connor, B., Dang, L.,
821 Doran, G., Fisher, B., Frankenberg, C., Fu, D., Granat, R., Hobbs, J., Lee, R. A. M.,
822 Mandrake, L., McDuffie, J., Miller, C. E., Myers, V., Natraj, V., O'Brien, D., Osterman, G.

823 B., Oyafuso, F., Payne, V. H., Pollock, H. R., Polonsky, I., Roehl, C. M., Rosenberg, R.,
824 Schwandner, F., Smyth, M., Tang, V., Taylor, T. E., To, C., Wunch, D., and Yoshimizu, J.:
825 The Orbiting Carbon Observatory-2: first 18 months of science data products, *Atmos. Meas.*
826 *Tech.*, 10, 549–563, <https://doi.org/10.5194/amt-10-549-2017>, 2017.

827 Eldering, A., Taylor, T. E., O'Dell, C. W., and Pavlick, R.: The OCO-3 mission:
828 measurement objectives and expected performance based on 1 year of simulated data, *Atmos.*
829 *Meas. Tech.*, 12, 2341–2370, <https://doi.org/10.5194/amt-12-2341-2019>, 2019.

830 Fan, N., & Forkel, M. (2025). Drivers of the enhanced amplitude of atmospheric CO₂ in
831 northern terrestrial ecosystems. <https://doi.org/10.5194/egusphere-egu25-7279>

832 Fang, S. X., Tans, P. P., Steinbacher, M., Zhou, L. X., and Luan, T.: Comparison of the
833 regional CO₂ mole fraction filtering approaches at a WMO/GAW regional station in China,
834 *Atmospheric Measurement Techniques*, 8, 5301–5313, [https://doi.org/10.5194/amt-8-5301-](https://doi.org/10.5194/amt-8-5301-2015)
835 2015, 2015.

836 Fawzy, S., Osman, A. I., Doran, J., and Rooney, D. W.: Strategies for mitigation of climate
837 change: a review, *Environ Chem Lett*, 18, 2069–2094, [https://doi.org/10.1007/s10311-020-](https://doi.org/10.1007/s10311-020-01059-w)
838 01059-w, 2020.

839 Frankenberg, C., O'Dell, C., Berry, J., Guanter, L., Joiner, J., Köhler, P., Pollock, R., and
840 Taylor, T. E.: Prospects for chlorophyll fluorescence remote sensing from the Orbiting
841 Carbon Observatory-2, *Remote Sensing of Environment*, 147, 1–12,
842 <https://doi.org/10.1016/j.rse.2014.02.007>, 2014.

843 Friedlingstein, P., O'Sullivan, M., Jones, M. W., Andrew, R. M., Hauck, J., Landschützer, P.,
844 Le Quéré, C., Li, H., Luijckx, I. T., Olsen, A., Peters, G. P., Peters, W., Pongratz, J.,
845 Schwingshackl, C., Sitch, S., Canadell, J. G., Ciais, P., Jackson, R. B., Alin, S. R., Arneeth, A.,
846 Arora, V., Bates, N. R., Becker, M., Bellouin, N., Berghoff, C. F., Bittig, H. C., Bopp, L.,
847 Cadule, P., Campbell, K., Chamberlain, M. A., Chandra, N., Chevallier, F., Chini, L. P.,
848 Colligan, T., Decayeux, J., Djeutchouang, L. M., Dou, X., Duran Rojas, C., Enyo, K., Evans,
849 W., Fay, A. R., Feely, R. A., Ford, D. J., Foster, A., Gasser, T., Gehlen, M., Gkritzalis, T.,
850 Grassi, G., Gregor, L., Gruber, N., Gürses, Ö., Harris, I., Hefner, M., Heinke, J., Hurtt, G. C.,
851 Iida, Y., Ilyina, T., Jacobson, A. R., Jain, A. K., Jarníková, T., Jersild, A., Jiang, F., Jin, Z.,
852 Kato, E., Keeling, R. F., Klein Goldewijk, K., Knauer, J., Korsbakken, J. I., Lan, X., Lauvset,
853 S. K., Lefèvre, N., Liu, Z., Liu, J., Ma, L., Maksyutov, S., Marland, G., Mayot, N., McGuire,
854 P. C., Metzl, N., Monacci, N. M., Morgan, E. J., Nakaoka, S.-I., Neill, C., Niwa, Y., Nützel,
855 T., Olivier, L., Ono, T., Palmer, P. I., Pierrot, D., Qin, Z., Resplandy, L., Roobaert, A.,
856 Rosan, T. M., Rödenbeck, C., Schwinger, J., Smallman, T. L., Smith, S. M., Sospedra-
857 Alfonso, R., Steinhoff, T., et al.: Global Carbon Budget 2024, *Earth Syst. Sci. Data*, 17, 965–
858 1039, <https://doi.org/10.5194/essd-17-965-2025>, 2025.

859 Halder, S., Tiwari, Y. K., Valsala, V., Sreeush, M. G., Sijikumar, S., Janardanan, R., &
860 Maksyutov, S. (2021). Quantification of enhancement in atmospheric CO₂ background due to
861 Indian biospheric fluxes and fossil fuel emissions. *Journal of Geophysical Research:*
862 *Atmospheres*, 126(13), e2021JD034545.

863 Harriss, R. C., Sachse, G. W., Collins Jr., J. E., Wade, L., Bartlett, K. B., Talbot, R. W.,
864 Browell, E. V., Barrie, L. A., Hill, G. F., and Burney, L. G.: Carbon monoxide and methane

865 over Canada: July–August 1990, *Journal of Geophysical Research: Atmospheres*, 99, 1659–
866 1669, <https://doi.org/10.1029/93JD01906>, 1994.

867 Huang, J., Golombek, A., Prinn, R., Weiss, R., Fraser, P., Simmonds, P., Dlugokencky, E. J.,
868 Hall, B., Elkins, J., Steele, P., Langenfelds, R., Krummel, P., Dutton, G., and Porter, L.:
869 Estimation of regional emissions of nitrous oxide from 1997 to 2005 using multinetwork
870 measurements, a chemical transport model, and an inverse method, *Journal of Geophysical
871 Research: Atmospheres*, 113, <https://doi.org/10.1029/2007JD009381>, 2008.

872 Huang, J., Yu, H., Guan, X., Wang, G., and Guo, R.: Accelerated dryland expansion under
873 climate change, *Nature Clim Change*, 6, 166–171, <https://doi.org/10.1038/nclimate2837>,
874 2016.

875 IPCC, 2021: *Climate Change 2021: The Physical Science Basis. Contribution of Working
876 Group I to the Sixth Assessment Report of the Intergovernmental Panel on Climate
877 Change*[Masson-Delmotte, V., P. Zhai, A. Pirani, S.L. Connors, C. Péan, S. Berger, N. Caud,
878 Y. Chen, L. Goldfarb, M.I. Gomis, M. Huang, K. Leitzell, E. Lonnoy, J.B.R. Matthews, T.K.
879 Maycock, T. Waterfield, O. Yelekçi, R. Yu, and B. Zhou (eds.)]. Cambridge University
880 Press, Cambridge, United Kingdom and New York, NY, USA, In press,
881 doi:10.1017/9781009157896.

882 Ito, A.: Disequilibrium of terrestrial ecosystem CO₂ budget caused by disturbance-induced
883 emissions and non-CO₂ carbon export flows: a global model assessment, *Earth Syst. Dynam.*,
884 10, 685–709, <https://doi.org/10.5194/esd-10-685-2019>, 2019.

885 Jain, C. D., Singh, V., Akhil Raj, S. T., Madhavan, B. L., and Ratnam, M. V.: Local emission
886 and long-range transport impacts on the CO, CO₂, and CH₄ concentrations at a tropical rural
887 site, *Atmospheric Environment*, 254, 118397,
888 <https://doi.org/10.1016/j.atmosenv.2021.118397>, 2021.

889 Jing, X., Huang, J., Wang, G., Higuchi, K., Bi, J., Sun, Y., Yu, H., and Wang, T.: The effects
890 of clouds and aerosols on net ecosystem CO₂ exchange over semi-arid Loess Plateau of
891 Northwest China, *Atmospheric Chemistry and Physics*, 10, 8205–8218,
892 <https://doi.org/10.5194/acp-10-8205-2010>, 2010.

893 Joiner, J. and Yoshida, Y.: Satellite-based reflectances capture large fraction of variability in
894 global gross primary production (GPP) at weekly time scales, *Agricultural and Forest
895 Meteorology*, 291, 108092, <https://doi.org/10.1016/j.agrformet.2020.108092>, 2020.

896 Joiner, J., Yoshida, Y., Zhang, Y., Duveiller, G., Jung, M., Lyapustin, A., Wang, Y., and
897 Tucker, C. J.: Estimation of Terrestrial Global Gross Primary Production (GPP) with Satellite
898 Data-Driven Models and Eddy Covariance Flux Data, *Remote Sensing*, 10, 1346,
899 <https://doi.org/10.3390/rs10091346>, 2018.

900 Jones, M. W., Andrew, R. M., Peters, G. P., Janssens-Maenhout, G., De-Gol, A. J., Ciais, P.,
901 Patra, P. K., Chevallier, F., and Le Quéré, C.: Gridded fossil CO₂ emissions and related O₂
902 combustion consistent with national inventories 1959–2018, *Sci Data*, 8, 2,
903 <https://doi.org/10.1038/s41597-020-00779-6>, 2021.

904 Kar, J., Bremer, H., Drummond, J. R., Rochon, Y. J., Jones, D. B. A., Nichitiu, F., Zou, J.,
905 Liu, J., Gille, J. C., Edwards, D. P., Deeter, M. N., Francis, G., Ziskin, D., and Warner, J.:

906 Evidence of vertical transport of carbon monoxide from Measurements of Pollution in the
907 Troposphere (MOPITT), *Geophysical Research Letters*, 31,
908 <https://doi.org/10.1029/2004GL021128>, 2004.

909 Krishnapriya, M., Pattanaik, D. R., Kumar, A., Ramana, M. V., & Naidu, C. V. (2025).
910 Spatio-temporal dynamics of atmospheric CO₂ over India and its inter-relationship with
911 combustion emissions, ecosystem exchange, and meteorological factors: M Krishnapriya et
912 al. *Journal of Earth System Science*, 134(4), 193.

913 Krol, M., Houweling, S., Bregman, B., van den Broek, M., Segers, A., van Velthoven, P.,
914 Peters, W., Dentener, F., and Bergamaschi, P.: The two-way nested global chemistry-
915 transport zoom model TM5: algorithm and applications, *Atmospheric Chemistry and Physics*
916 *Discussions*, 4, 3975–4018, 2004.

917 Kumar, A., Yu, Z.-G., Klemeš, J. J., and Bokhari, A.: A state-of-the-art review of greenhouse
918 gas emissions from Indian hydropower reservoirs, *Journal of Cleaner Production*, 320,
919 128806, <https://doi.org/10.1016/j.jclepro.2021.128806>, 2021.

920 Kunchala, R. K., Girach, I., Das, C., Jain, C., Burman, P. K. D., Pathakoti, M., ... & Jain, V.
921 (2025). Carbon dioxide (CO₂) variations across India: Synthesis of observations and model
922 simulations. *Atmospheric Environment*, 121746.

923 Kunchala, R. K., Patra, P. K., Kumar, K. N., Chandra, N., Attada, R., and Karumuri, R. K.:
924 Spatio-temporal variability of XCO₂ over Indian region inferred from Orbiting Carbon
925 Observatory (OCO-2) satellite and Chemistry Transport Model, *Atmospheric Research*, 269,
926 106044, <https://doi.org/10.1016/j.atmosres.2022.106044>, 2022.

927 Kuttippurath, J., Peter, R., Singh, A., and Raj, S.: The increasing atmospheric CO₂ over
928 India: Comparison to global trends, *iScience*, 25, 104863,
929 <https://doi.org/10.1016/j.isci.2022.104863>, 2022.

930 Lai, S. C., Baker, A. K., Schuck, T. J., van Velthoven, P., Oram, D. E., Zahn, A., Hermann,
931 M., Weigelt, A., Slemr, F., Brenninkmeijer, C. a. M., and Ziereis, H.: Pollution events
932 observed during CARIBIC flights in the upper troposphere between South China and the
933 Philippines, *Atmospheric Chemistry and Physics*, 10, 1649–1660,
934 <https://doi.org/10.5194/acp-10-1649-2010>, 2010.

935 Le Quéré, C., Andrew, R. M., Friedlingstein, P., Sitch, S., Pongratz, J., Manning, A. C.,
936 Korsbakken, J. I., Peters, G. P., Canadell, J. G., Jackson, R. B., Boden, T. A., Tans, P. P.,
937 Andrews, O. D., Arora, V. K., Bakker, D. C. E., Barbero, L., Becker, M., Betts, R. A., Bopp,
938 L., Chevallier, F., Chini, L. P., Ciais, P., Cosca, C. E., Cross, J., Currie, K., Gasser, T., Harris,
939 I., Hauck, J., Haverd, V., Houghton, R. A., Hunt, C. W., Hurtt, G., Ilyina, T., Jain, A. K.,
940 Kato, E., Kautz, M., Keeling, R. F., Klein Goldewijk, K., Körtzinger, A., Landschützer, P.,
941 Lefèvre, N., Lenton, A., Lienert, S., Lima, I., Lombardozzi, D., Metzl, N., Millero, F.,
942 Monteiro, P. M. S., Munro, D. R., Nabel, J. E. M. S., Nakaoka, S., Nojiri, Y., Padin, X. A.,
943 Pregon, A., Pfeil, B., Pierrot, D., Poulter, B., Rehder, G., Reimer, J., Rödenbeck, C.,
944 Schwinger, J., Séférian, R., Skjelvan, I., Stocker, B. D., Tian, H., Tilbrook, B., Tubiello, F.
945 N., Van Der Laan-Luijkx, I. T., Van Der Werf, G. R., Van Heuven, S., Viovy, N., Vuichard,
946 N., Walker, A. P., Watson, A. J., Wiltshire, A. J., Zaehle, S., and Zhu, D.: Global Carbon
947 Budget 2017, *Earth Syst. Sci. Data*, 10, 405–448, <https://doi.org/10.5194/essd-10-405-2018>,
948 2018.

949 [ICOS RI, 2020. ICOS Atmosphere Station Specifications, V2.0 \(editor: O. Laurent\). ICOS](#)
950 [ERIC. <https://doi.org/10.18160/GK28-2188>](#)
951
952 Lin, X., Indira, N. K., Ramonet, M., Delmotte, M., Ciais, P., Bhatt, B. C., Reddy, M. V.,
953 Angchuk, D., Balakrishnan, S., Jorphail, S., Dorjai, T., Mahey, T. T., Patnaik, S., Begum, M.,
954 Brenninkmeijer, C., Durairaj, S., Kirubakaran, R., Schmidt, M., Swathi, P. S., Vinithkumar,
955 N. V., Yver Kwok, C., and Gaur, V. K.: Long-lived atmospheric trace gases measurements in
956 flask samples from three stations in India, *Atmos. Chem. Phys.*, 15, 9819–9849,
957 <https://doi.org/10.5194/acp-15-9819-2015>, 2015.

958 Lin, X., Ciais, P., Bousquet, P., Ramonet, M., Yin, Y., Balkanski, Y., Cozic, A., Delmotte,
959 M., Evangeliou, N., Indira, N. K., Locatelli, R., Peng, S., Piao, S., Saunio, M., Swathi, P. S.,
960 Wang, R., Yver-Kwok, C., Tiwari, Y. K., and Zhou, L.: Simulating CH₄ and CO₂ over South
961 and East Asia using the zoomed chemistry transport model LMDz-INCA, *Atmos. Chem.*
962 *Phys.*, 18, 9475–9497, <https://doi.org/10.5194/acp-18-9475-2018>, 2018.

963 Liu, J., Bowman, K. W., Lee, M., Henze, D. K., Bousserez, N., Brix, H., Collatz, G. J.,
964 Menemenlis, D., Ott, L., Pawson, S., Jones, D., and Nassar, R.: Carbon monitoring system
965 flux estimation and attribution: impact of ACOS-GOSAT XCO₂ sampling on the inference of
966 terrestrial biospheric sources and sinks, *Tellus B: Chemical and Physical Meteorology*, 66,
967 22486, <https://doi.org/10.3402/tellusb.v66.22486>, 2014.

968 Lopez, M.: Estimation des émissions de gaz à effet de serre à différentes échelles en France à
969 l'aide d'observations de haute précision, phdthesis, Université Paris Sud - Paris XI, 2012.

970 Mahesh, P., Sreenivas, G., Rao, P. V. N., Dadhwal, V. K., Sai Krishna, S. V. S., and
971 Mallikarjun, K.: High-precision surface-level CO₂ and CH₄ using off-axis integrated cavity
972 output spectroscopy (OA-ICOS) over Shadnagar, India, *International Journal of Remote*
973 *Sensing*, 36, 5754–5765, <https://doi.org/10.1080/01431161.2015.1104744>, 2015.

974 [Mangaraj, P., Matsumi, Y., Nakayama, T., Biswal, A., Yamaji, K., Araki, H., ... & Mor, S.](#)
975 [\(2025\). Weak coupling of observed surface PM2.5 in Delhi-NCR with rice crop residue](#)
976 [burning in Punjab and Haryana. *Npj Climate and Atmospheric Science*, 8\(1\), 18.](#)

977 Masarie, K. A., Peters, W., Jacobson, A. R., and Tans, P. P.: ObsPack: a framework for the
978 preparation, delivery, and attribution of atmospheric greenhouse gas measurements, *Earth*
979 *Syst. Sci. Data*, 6, 375–384, <https://doi.org/10.5194/essd-6-375-2014>, 2014.

980 Matsueda, H., Inoue, H. Y., Ishii, M., and Tsutsumi, Y.: Large injection of carbon monoxide
981 into the upper troposphere due to intense biomass burning in 1997, *J. Geophys. Res.*, 104,
982 26867–26879, <https://doi.org/10.1029/1999JD900193>, 1999.

983 Mauzerall, D. L., Logan, J. A., Jacob, D. J., Anderson, B. E., Blake, D. R., Bradshaw, J. D.,
984 Heikes, B., Sachse, G. W., Singh, H., and Talbot, B.: Photochemistry in biomass burning
985 plumes and implications for tropospheric ozone over the tropical South Atlantic, *J. Geophys.*
986 *Res.*, 103, 8401–8423, <https://doi.org/10.1029/97JD02612>, 1998.

987 Metya, A., Datye, A., Chakraborty, S., Tiwari, Y. K., Sarma, D., Bora, A., and Gogoi, N.:
988 Diurnal and seasonal variability of CO₂ and CH₄ concentration in a semi-urban environment
989 of western India, *Sci Rep*, 11, 2931, <https://doi.org/10.1038/s41598-021-82321-1>, 2021.

Deleted: Laurent, O., 2016.

Deleted: Atmospheric

Deleted: .

Formatted: Space After: 0 pt, Border: Top: (No border),
Bottom: (No border), Left: (No border), Right: (No border),
Between : (No border)

- 993 Mühle, J., Brenninkmeijer, C. a. M., Rhee, T. S., Slemr, F., Oram, D. E., Penkett, S. A., and
 994 Zahn, A.: Biomass burning and fossil fuel signatures in the upper troposphere observed
 995 during a CARIBIC flight from Namibia to Germany, *Geophysical Research Letters*, 29, 16-1-
 996 16-4, <https://doi.org/10.1029/2002GL015764>, 2002.
- 997 Munksgaard, N. C., Lee, I. L., Napier, T. P., Zwart, C., Cernusak, L. A., & Bird, M. I. (2022).
 998 One year of spectroscopic high-frequency measurements of atmospheric CO₂, CH₄, H.
 999 *Geoscience Data Journal*. <https://doi.org/10.1002/gdj3.180>
- 1000 Nalini, K., Sijikumar, S., Valsala, V., Tiwari, Y. K., and Ramachandran, R.: Designing
 1001 surface CO₂ monitoring network to constrain the Indian land fluxes, *Atmospheric*
 1002 *Environment*, 218, 117003, <https://doi.org/10.1016/j.atmosenv.2019.117003>, 2019.
- 1003 Nath, B.: Quantitative Assessment of Forest Cover Change of a Part of Bandarban Hill Tracts
 1004 Using NDVI Techniques, *Journal of Geosciences and Geomatics*, 2, 21–27,
 1005 <https://doi.org/10.12691/jgg-2-1-4>, 2014.
- 1006 Nishanth, T., Praseed, K. M., Kumar, M. K. S., and Valsaraj, K. T.: Observational Study of
 1007 Surface O₃, NO_x, CH₄ and Total NMHCs at Kannur, India, *Aerosol Air Qual. Res.*, 14,
 1008 1074–1088, <https://doi.org/10.4209/aaqr.2012.11.0323>, 2014.
- 1009 Niwa, Y., Machida, T., Sawa, Y., Matsueda, H., Schuck, T. J., Brenninkmeijer, C. A. M.,
 1010 Imasu, R., and Satoh, M.: Imposing strong constraints on tropical terrestrial CO₂ fluxes using
 1011 passenger aircraft based measurements, *Journal of Geophysical Research: Atmospheres*, 117,
 1012 <https://doi.org/10.1029/2012JD017474>, 2012.
- 1013 Nomura, S., Naja, M., Ahmed, M. K., Mukai, H., Terao, Y., Machida, T., Sasakawa, M., and
 1014 Patra, P. K.: Measurement report: Regional characteristics of seasonal and long-term
 1015 variations in greenhouse gases at Nainital, India, and Comilla, Bangladesh, *Atmos. Chem.*
 1016 *Phys.*, 21, 16427–16452, <https://doi.org/10.5194/acp-21-16427-2021>, 2021.
- 1017 Paris, J.-D., Ciais, P., Nédélec, P., Ramonet, M., Belan, B. D., Arshinov, M. Yu., Golitsyn, G.
 1018 S., Granberg, I., Stohl, A., Cayez, G., Athier, G., Boumard, F., and Cousin, J.-M.: The YAK-
 1019 AEROSIB transcontinental aircraft campaigns: new insights on the transport of CO₂, CO and
 1020 O₃ across Siberia, *Tellus B: Chemical and Physical Meteorology*, 60, 551–568,
 1021 <https://doi.org/10.1111/j.1600-0889.2008.00369.x>, 2008.
- 1022 Park, M., Randel, W. J., Emmons, L. K., and Livesey, N. J.: Transport pathways of carbon
 1023 monoxide in the Asian summer monsoon diagnosed from Model of Ozone and Related
 1024 Tracers (MOZART), *J. Geophys. Res.*, 114, 2008JD010621,
 1025 <https://doi.org/10.1029/2008JD010621>, 2009.
- 1026 Pathakoti, M., D.V., M., Gaddamidi, S., Arun, S. S., Bothale, R. V., Chauhan, P., P, R., K.S.,
 1027 R., and Chandra, N.: Three-dimensional view of CO₂ variability in the atmosphere over the
 1028 Indian region, *Atmospheric Research*, 290, 106785,
 1029 <https://doi.org/10.1016/j.atmosres.2023.106785>, 2023.
- 1030 Patil, M. N., Dharmaraj, T., Waghmare, R. T., Prabha, T. V., and Kulkarni, J. R.:
 1031 Measurements of carbon dioxide and heat fluxes during monsoon-2011 season over rural site
 1032 of India by eddy covariance technique, *J Earth Syst Sci*, 123, 177–185,
 1033 <https://doi.org/10.1007/s12040-013-0374-z>, 2014.

1034 Patra, P. K., Niwa, Y., Schuck, T. J., Brenninkmeijer, C. a. M., Machida, T., Matsueda, H.,
 1035 and Sawa, Y.: Carbon balance of South Asia constrained by passenger aircraft CO₂
 1036 measurements, *Atmospheric Chemistry and Physics*, 11, 4163–4175,
 1037 <https://doi.org/10.5194/acp-11-4163-2011>, 2011.

1038 Patra, P. K., Canadell, J. G., Houghton, R. A., Piao, S. L., Oh, N.-H., Ciais, P., Manjunath, K.
 1039 R., Chhabra, A., Wang, T., Bhattacharya, T., Bousquet, P., Hartman, J., Ito, A., Mayorga, E.,
 1040 Niwa, Y., Raymond, P. A., Sarma, V. V. S. S., and Lasco, R.: The carbon budget of South
 1041 Asia, *Biogeosciences*, 10, 513–527, <https://doi.org/10.5194/bg-10-513-2013>, 2013.

1042 Patra, P. K., Crisp, D., Kaiser, J. W., Wunch, D., Saeki, T., Ichii, K., Sekiya, T., Wennberg,
 1043 P. O., Feist, D. G., Pollard, D. F., Griffith, D. W. T., Velazco, V. A., De Maziere, M., Sha, M.
 1044 K., Roehl, C., Chatterjee, A., and Ishijima, K.: The Orbiting Carbon Observatory (OCO-2)
 1045 tracks 2–3 peta-gram increase in carbon release to the atmosphere during the 2014–2016 El
 1046 Niño, *Sci Rep*, 7, 13567, <https://doi.org/10.1038/s41598-017-13459-0>, 2017.

1047 Patra, P. K., Takigawa, M., Watanabe, S., Chandra, N., Ishijima, K., and Yamashita, Y.:
 1048 Improved Chemical Tracer Simulation by MIROC4.0-based Atmospheric Chemistry-
 1049 Transport Model (MIROC4-ACTM), *Sola*, 14, 91–96, <https://doi.org/10.2151/sola.2018-016>,
 1050 2018.

1051 Peters, W., Miller, J. B., Whitaker, J., Denning, A. S., Hirsch, A., Krol, M. C., Zupanski, D.,
 1052 Bruhwiler, L., and Tans, P. P.: An ensemble data assimilation system to estimate CO₂ surface
 1053 fluxes from atmospheric trace gas observations, *Journal of Geophysical Research:
 1054 Atmospheres*, 110, <https://doi.org/10.1029/2005JD006157>, 2005.

1055 Philip, S., Johnson, M. S., Potter, C., Genovesse, V., Baker, D. F., Haynes, K. D., Henze, D.
 1056 K., Liu, J., and Poulter, B.: Prior biosphere model impact on global terrestrial CO₂ fluxes
 1057 estimated from OCO-2 retrievals, *Atmos. Chem. Phys.*, 19, 13267–13287,
 1058 <https://doi.org/10.5194/acp-19-13267-2019>, 2019.

1059 Philip, S., Johnson, M. S., Baker, D. F., Basu, S., Tiwari, Y. K., Indira, N. K., Ramonet, M.,
 1060 and Poulter, B.: OCO-2 Satellite-Imposed Constraints on Terrestrial Biospheric CO₂ Fluxes
 1061 Over South Asia, *JGR Atmospheres*, 127, e2021JD035035,
 1062 <https://doi.org/10.1029/2021JD035035>, 2022.

1063 Potter, C. S., Randerson, J. T., Field, C. B., Matson, P. A., Vitousek, P. M., Mooney, H. A.,
 1064 and Klooster, S. A.: Terrestrial ecosystem production: A process model based on global
 1065 satellite and surface data, *Global Biogeochemical Cycles*, 7, 811–841,
 1066 <https://doi.org/10.1029/93GB02725>, 1993.

1067 Randel, W. J. and Park, M.: Deep convective influence on the Asian summer monsoon
 1068 anticyclone and associated tracer variability observed with Atmospheric Infrared Sounder
 1069 (AIRS), *Journal of Geophysical Research: Atmospheres*, 111,
 1070 <https://doi.org/10.1029/2005JD006490>, 2006.

1071 Randerson, J. T., Thompson, M. V., Conway, T. J., Fung, I. Y., and Field, C. B.: The
 1072 contribution of terrestrial sources and sinks to trends in the seasonal cycle of atmospheric
 1073 carbon dioxide, *Global Biogeochemical Cycles*, 11, 535–560,
 1074 <https://doi.org/10.1029/97GB02268>, 1997.

- 1075 Rathore, J., Ganguly, D., Singh, V., Gupta, M., Vazhathara, V. J., Biswal, A., Kunchala, R.
 1076 K., Patra, P. K., Sahu, L. K., Gani, S., and Dey, S.: Characteristics of Haze Pollution Events
 1077 During Biomass Burning Period at an Upwind Site of Delhi, *JGR Atmospheres*, 130,
 1078 e2024JD042347, <https://doi.org/10.1029/2024JD042347>, 2025.
- 1079 Rayner, P. J., Law, R. M., Allison, C. E., Francey, R. J., Trudinger, C. M., and Pickett-Heaps,
 1080 C.: Interannual variability of the global carbon cycle (1992–2005) inferred by inversion of
 1081 atmospheric CO₂ and δ¹³CO₂ measurements, *Global Biogeochemical Cycles*, 22,
 1082 <https://doi.org/10.1029/2007GB003068>, 2008.
- 1083 Reid, K. H. and Steyn, D. G.: Diurnal variations of boundary-layer carbon dioxide in a
 1084 coastal city—Observations and comparison with model results, *Atmospheric Environment*,
 1085 31, 3101–3114, [https://doi.org/10.1016/S1352-2310\(97\)00050-2](https://doi.org/10.1016/S1352-2310(97)00050-2), 1997.
- 1086 Russo, R. S., Talbot, R. W., Dibb, J. E., Scheuer, E., Seid, G., Jordan, C. E., Fuelberg, H. E.,
 1087 Sachse, G. W., Avery, M. A., Vay, S. A., Blake, D. R., Blake, N. J., Atlas, E., Fried, A.,
 1088 Sandholm, S. T., Tan, D., Singh, H. B., Snow, J., and Heikes, B. G.: Chemical composition
 1089 of Asian continental outflow over the western Pacific: Results from Transport and Chemical
 1090 Evolution over the Pacific (TRACE-P), *Journal of Geophysical Research: Atmospheres*, 108,
 1091 <https://doi.org/10.1029/2002JD003184>, 2003.
- 1092 Sawa, Y., Matsueda, H., Makino, Y., Inoue, H. Y., Murayama, S., Hirota, M., Tsutsumi, Y.,
 1093 Zaizen, Y., Ikegami, M., and Okada, K.: Aircraft Observation of CO₂, CO₂ O₃ and H₂ over
 1094 the North Pacific during the PACE-7 Campaign, *Tellus B: Chemical and Physical*
 1095 *Meteorology*, 56, 2, <https://doi.org/10.3402/tellusb.v56i1.16402>, 2004.
- 1096 Schaaf, C. and Wang, Z.: MODIS/Terra+Aqua BRDF/Albedo Nadir BRDF-Adjusted Ref
 1097 Band6 Daily L3 Global 30ArcSec CMG V061,
 1098 <https://doi.org/10.5067/MODIS/MCD43D67.061>, 2021.
- 1099 Schaaf, C. B., Gao, F., Strahler, A. H., Lucht, W., Li, X., Tsang, T., Strugnell, N. C., Zhang,
 1100 X., Jin, Y., Muller, J.-P., Lewis, P., Barnsley, M., Hobson, P., Disney, M., Roberts, G.,
 1101 Dunderdale, M., Doll, C., d'Entremont, R. P., Hu, B., Liang, S., Privette, J. L., and Roy, D.:
 1102 First operational BRDF, albedo nadir reflectance products from MODIS, *Remote Sensing of*
 1103 *Environment*, 83, 135–148, [https://doi.org/10.1016/S0034-4257\(02\)00091-3](https://doi.org/10.1016/S0034-4257(02)00091-3), 2002.
- 1104 Schuck, T. J., Ishijima, K., Patra, P. K., Baker, A. K., Machida, T., Matsueda, H., Sawa, Y.,
 1105 Umezawa, T., Brenninkmeijer, C. a. M., and Lelieveld, J.: Distribution of methane in the
 1106 tropical upper troposphere measured by CARIBIC and CONTRAIL aircraft, *Journal of*
 1107 *Geophysical Research: Atmospheres*, 117, <https://doi.org/10.1029/2012JD018199>, 2012.
- 1108 Schuldt, K. N., Mund, J., Aalto, T., Abshire, J. B., Aikin, K., Allen, G., Andrade, M., Arlyn
 1109 Andrews, Apadula, F., Arnold, S., Baier, B., Bakwin, P., Bani, L., Bartyzel, J., Bentz, G.,
 1110 Bergamaschi, P., Beyersdorf, A., Biermann, T., Biraud, S. C., Pierre-Eric Blanc, Boenisch,
 1111 H., Bowling, D., Brailsford, G., Brand, W. A., Brunner, D., Bui, T. P. V., Van Den Bulk, P.,
 1112 Benoit Burban, Francescopiero Calzolari, Chang, C. S., Chen, G., Huilin Chen, Lukasz
 1113 Chmura, St. Clair, J. M., Clark, S., Sites Climadat, Coletta, J. D., Colomb, A., Commane, R.,
 1114 Condori, L., Conen, F., Conil, S., Couret, C., Cristofanelli, P., Cuevas, E., Curcoll, R., Daube,
 1115 B., Davis, K. J., Dean-Day, J. M., Delmotte, M., Dickerson, R., DiGangi, E., DiGangi, J. P.,
 1116 Van Dinter, D., Elsasser, M., Emmenegger, L., Shuangxi Fang, Forster, G., France, J.,
 1117 Frumau, A., Fuente-Lastra, M., Galkowski, M., Gatti, L. V., Gehrlein, T., Gerbig, C.,

- 1118 Francois Gheusi, Gloor, E., Goto, D., Griffis, T., Hammer, S., Hanisco, T. F., Hanson, C.,
1119 Haszpra, L., Hatakka, J., Heimann, M., Heliasz, M., Heltai, D., Henne, S., Hensen, A.,
1120 Hermans, C., Hermansen, O., Hintsa, E., Hoheisel, A., Holst, J., Di Iorio, T., Iraci, L. T.,
1121 Ivakhov, V., Jaffe, D. A., Jordan, A., Joubert, W., Kang, H.-Y., Karion, A., Kawa, S. R.,
1122 Kazan, V., Keeling, R. F., Keronen, P., Jooil Kim, Klausen, J., Kneuer, T., et al.: Multi-
1123 laboratory compilation of atmospheric carbon dioxide data for the period 1957-2023;
1124 obspack_co2_1_GLOBALVIEWplus_v10.1_2024-11-13,
1125 <https://doi.org/10.25925/20241101>, 2024.
- 1126 Sharma, N., Dadhwal, V. K., Kant, Y., Mahesh, P., Mallikarjun, K., Gadavi, H., Sharma, A.,
1127 and Ali, M. M.: Atmospheric CO₂ Variations in Two Contrasting Environmental Sites Over
1128 India, *Air, Soil and Water Research*, 7, ASWR.S13987,
1129 <https://doi.org/10.4137/ASWR.S13987>, 2014.
- 1130 Sreenivas, G., Mahesh, P., Subin, J., Kanchana, A. L., Rao, P. V. N., and Dadhwal, V. K.:
1131 Influence of Meteorology and interrelationship with greenhouse gases
1132 (CO₂ and CH₄) at a suburban site of India,
1133 *Atmos. Chem. Phys.*, 16, 3953–3967, <https://doi.org/10.5194/acp-16-3953-2016>, 2016.
- 1134 Sreenivas, G., P. M., Mahalakshmi, D. V., Kanchana, A. L., Chandra, N., Patra, P. K., Raja,
1135 P., Sesha Sai, M. V. R., Sripada, S., Rao, P. V. N., and Dadhwal, V. K.: Seasonal and annual
1136 variations of CO₂ and CH₄ at Shadnagar, a semi-urban site, *Science of The Total
1137 Environment*, 819, 153114, <https://doi.org/10.1016/j.scitotenv.2022.153114>, 2022.
- 1138 Srivastava, P., Bennett, M. W., Bedrosian, G., Rosenberg, R., Solish, B., and Basilio, R. R.:
1139 Establishing Launch Readiness of NASA ISS Instrument OCO-3, in: *IGARSS 2020 - 2020
1140 IEEE International Geoscience and Remote Sensing Symposium, IGARSS 2020 - 2020 IEEE
1141 International Geoscience and Remote Sensing Symposium, Waikoloa, HI, USA, 6101–6104,
1142 https://doi.org/10.1109/IGARSS39084.2020.9323631*, 2020.
- 1143 Stocker, T.F., D. Qin, G.-K. Plattner, L.V. Alexander, S.K. Allen, N.L. Bindoff, F.-M. Bréon,
1144 J.A. Church, U. Cubasch, S. Emori, P. Forster, P. Friedlingstein, N. Gillett, J.M. Gregory,
1145 D.L. Hartmann, E. Jansen, B. Kirtman, R. Knutti, K. Krishna Kumar, P. Lemke, J. Marotzke,
1146 V.Masson-Delmotte, G.A. Meehl, I.I. Mokhov, S. Piao, V. Ramaswamy, D. Randall, M.
1147 Rhein, M. Rojas, C. Sabine, D. Shindell, L.D. Talley, D.G. Vaughan and S.-P. Xie, 2013:
1148 Technical Summary. In: *Climate Change 2013: The Physical Science Basis. Contribution of
1149 Working Group I to the Fifth Assessment Report of the Intergovernmental Panel on Climate
1150 Change* [Stocker, T.F., D. Qin, G.-K. Plattner, M. Tignor, S.K. Allen, J. Boschung, A.
1151 Nauels, Y. Xia, V. Bex and P.M. Midgley (eds.)]. Cambridge University Press, Cambridge,
1152 United Kingdom and New York, NY, USA
- 1153 Stull, R. B. (Ed.): *An Introduction to Boundary Layer Meteorology*, Springer Netherlands,
1154 Dordrecht, <https://doi.org/10.1007/978-94-009-3027-8>, 1988.
- 1155 Summa, D., Di Girolamo, P., Stelitalo, D., and Cacciani, M.: Characterization of the
1156 planetary boundary layer height and structure by Raman lidar: comparison of different
1157 approaches, *Atmospheric Measurement Techniques*, 6, 3515–3525,
1158 <https://doi.org/10.5194/amt-6-3515-2013>, 2013.
- 1159 Sun, Y., Frankenberg, C., Jung, M., Joiner, J., Guanter, L., Köhler, P., and Magney, T.:
1160 Overview of Solar-Induced chlorophyll Fluorescence (SIF) from the Orbiting Carbon

- 1161 Observatory-2: Retrieval, cross-mission comparison, and global monitoring for GPP, Remote
1162 Sensing of Environment, 209, 808–823, <https://doi.org/10.1016/j.rse.2018.02.016>, 2018.
- 1163 Thilakan, V., Pillai, D., Sukumaran, J., Gerbig, C., Hakkim, H., Sinha, V., Terao, Y., Naja,
1164 M., and Deshpande, M. V.: Potential of using CO₂ observations over India in regional carbon
1165 budget estimation by improving the modelling system, EGU sphere, 1–32,
1166 <https://doi.org/10.5194/egusphere-2023-1582>, 2023.
- 1167 Tiwari, Y., Valsala, V., Vellore, R., and Kunchala, R.: Effectiveness of surface monitoring
1168 stations in representing regional CO₂ emissions over India, Clim. Res., 56, 121–129,
1169 <https://doi.org/10.3354/cr01149>, 2013.
- 1170 Tiwari, Y. K., Vellore, R. K., Ravi Kumar, K., Van Der Schoot, M., and Cho, C.-H.:
1171 Influence of monsoons on atmospheric CO₂ spatial variability and ground-based monitoring
1172 over India, Science of The Total Environment, 490, 570–578,
1173 <https://doi.org/10.1016/j.scitotenv.2014.05.045>, 2014.
- 1174 Vermote, E. and NOAA CDR Program: NOAA Climate Data Record (CDR) of AVHRR
1175 Normalized Difference Vegetation Index (NDVI), Version 5,
1176 <https://doi.org/10.7289/V5ZG6QH9>, 2018.
- 1177 Wada, A., Matsueda, H., Sawa, Y., Tsuboi, K., and Okubo, S.: Seasonal variation of
1178 enhancement ratios of trace gases observed over 10 years in the western North Pacific,
1179 Atmospheric Environment, 45, 2129–2137, <https://doi.org/10.1016/j.atmosenv.2011.01.043>,
1180 2011.
- 1181 Wang, G., Huang, J., Guo, W., Zuo, J., Wang, J., Bi, J., Huang, Z., and Shi, J.: Observation
1182 analysis of land-atmosphere interactions over the Loess Plateau of northwest China, Journal
1183 of Geophysical Research: Atmospheres, 115, <https://doi.org/10.1029/2009JD013372>, 2010.
- 1184 Wang, Z., Schaaf, C. B., Sun, Q., Shuai, Y., and Román, M. O.: Capturing rapid land surface
1185 dynamics with Collection V006 MODIS BRDF/NBAR/Albedo (MCD43) products, Remote
1186 Sensing of Environment, 207, 50–64, <https://doi.org/10.1016/j.rse.2018.02.001>, 2018.
- 1187 Watanabe, S., Miura, H., Sekiguchi, M., Nagashima, T., Sudo, K., Emori, S., and Kawamiya,
1188 M.: Development of an atmospheric general circulation model for integrated Earth system
1189 modeling on the Earth Simulator, Earth Simulator, 9, 27–35, 2008.
- 1190 Wigley, T. M. L. (1983). The pre-industrial carbon dioxide level. *Climatic change*, 5(4), 315-
1191 320.
- 1192 Worthy, D. E. J., Chan, E., Ishizawa, M., Chan, D., Poss, C., Dlugokencky, E. J., Maksyutov,
1193 S., and Levin, I.: Decreasing anthropogenic methane emissions in Europe and Siberia inferred
1194 from continuous carbon dioxide and methane observations at Alert, Canada, Journal of
1195 Geophysical Research: Atmospheres, 114, <https://doi.org/10.1029/2008JD011239>, 2009.
- 1196 Xiao, Y., Jacob, D. J., Wang, J. S., Logan, J. A., Palmer, P. I., Suntharalingam, P., Yantosca,
1197 R. M., Sachse, G. W., Blake, D. R., and Streets, D. G.: Constraints on Asian and European
1198 sources of methane from CH₄-C₂H₆-CO correlations in Asian outflow, J. Geophys. Res.,
1199 109, 2003JD004475, <https://doi.org/10.1029/2003JD004475>, 2004.

- 1200 Xiong, X., Houweling, S., Wei, J., Maddy, E., Sun, F., and Barnet, C.: Methane plume over
1201 south Asia during the monsoon season: satellite observation and model simulation,
1202 Atmospheric Chemistry and Physics, 9, 783–794, <https://doi.org/10.5194/acp-9-783-2009>,
1203 2009.
- 1204 Yoro, K. O. and Daramola, M. O.: CO₂ emission sources, greenhouse gases, and the global
1205 warming effect, in: Advances in Carbon Capture, Elsevier, 3–28,
1206 <https://doi.org/10.1016/B978-0-12-819657-1.00001-3>, 2020.
- 1207 Yuan, Y., Ries, L., Petermeier, H., Steinbacher, M., Gómez-Peláez, A. J., Leuenberger, M.
1208 C., Schumacher, M., Trickl, T., Couret, C., Meinhardt, F., and Menzel, A.: Adaptive selection
1209 of diurnal minimum variation: a statistical strategy to obtain representative atmospheric CO₂
1210 data and its application to European elevated mountain stations, Atmospheric Measurement
1211 Techniques, 11, 1501–1514, <https://doi.org/10.5194/amt-11-1501-2018>, 2018.
- 1212 Zhang, H. F., Chen, B. Z., van der Laan-Luijk, I. T., Machida, T., Matsueda, H., Sawa, Y.,
1213 Fukuyama, Y., Langenfelds, R., van der Schoot, M., Xu, G., Yan, J. W., Cheng, M. L., Zhou,
1214 L. X., Tans, P. P., and Peters, W.: Estimating Asian terrestrial carbon fluxes from
1215 CONTRAIL aircraft and surface CO₂ observations for the period 2006–2010,
1216 Atmospheric Chemistry and Physics, 14, 5807–5824, [https://doi.org/10.5194/acp-14-5807-](https://doi.org/10.5194/acp-14-5807-2014)
1217 2014, 2014.
- 1218 Zhang, X., Nakazawa, T., Ishizawa, M., Aoki, S., Nakaoka, S.-I., Sugawara, S., Maksyutov,
1219 S., Saeki, T., and Hayasaka, T.: Temporal variations of atmospheric carbon dioxide in the
1220 southernmost part of Japan, Tellus B: Chemical and Physical Meteorology, 59, 654–663,
1221 <https://doi.org/10.1111/j.1600-0889.2007.00288.x>, 2007.
- 1222